

Dr. Sameer Mulani

Co-PI

Two papers:

- Wing-Box Weight Optimization Using Curvilinear Spars and Ribs (SpaRibs)
- Nonstationary Random Vibration Analysis of Wing with Geometric Nonlinearity Under Correlated Excitation



Wing-Box Weight Optimization Using Curvilinear Spars and Ribs (SpaRibs)

Davide Locatelli,* Sameer B. Mulani,† and Rakesh K. Kapania‡

Virginia Polytechnic Institute and State University, Blacksburg, Virginia 24061-0203

DOI: 10.2514/1.C031336

The aim of this research is to perform topology and sizing optimization of wing-box structures using curvilinear spars and ribs, referred to as *SpaRibs* in the following. To accomplish this, a new framework called *EBF3SSWingOpt* is being developed at Virginia Polytechnic Institute and State University. The optimization framework includes two different methodologies: a one-step optimization methodology where topology and sizing optimization are carried out together and a two-step optimization methodology where topology and sizing optimization are carried out separately using different constraints and objective functions. A description of how the general framework is developed and applied for optimizing winglike structures is provided and the optimization-problem formulation is stated. Two practical design problems solved using *EBF3SSWingOpt* are presented: a rectangular wing box and a generic fighter wing. In both cases, the structure with the *SpaRibs* is lighter than the initial structure with straight spars and ribs. Moreover, the two-step optimization framework has proven to be better at finding an optimal solution than the one-step framework. Finally, different designs with comparable weights but different stress distributions, buckling properties, and dynamic behaviors were found.

Nomenclature

A_i	=	i th finite element area
BF_0	=	buckling factor
EBF^3	=	electron beam free-form fabrication
$f(\mathbf{x})$	=	optimization objective function
$g_i(\mathbf{x})$	=	i th optimization constraint function
KSC_σ	=	Kreisselmeier–Steinhauser stress coefficient
n_{iter}	=	number of iterations
P	=	applied load
P_{cr}	=	critical buckling load
SF	=	safety factor
T_{CPU}	=	CPU time
W	=	weight
W_{MAX}	=	maximum weight
\mathbf{x}	=	design-variable vector
x_{jMAX}	=	j th design-variable upper boundary
x_{jmin}	=	j th design-variable lower boundary
λ_0	=	fundamental buckling eigenvalue
ρ	=	Kreisselmeier–Steinhauser constant
σ_i	=	i th finite element von Mises stress
σ_u	=	ultimate tension stress
σ_{VM}	=	von Mises stress
σ_y	=	yield stress of the material

I. Introduction

THE present work is motivated by the fact that to enhance structural performance in aerospace field, new design concepts for aircraft structures are needed. Two aspects are of particular

interest for industry and manufacturing: bring design optimization and high-fidelity analysis in the early stages of design and bring together as many disciplines as possible. The quest for the best design is dictated by many constraints related to environmental issues, manufacturing time and cost, maintenance cost, and operational cost, which have to be added to the typical structural integrity and safety constraints. As a consequence, nowadays, engineers are challenged to take into account all these aspects during the early stages of concept design, and they need new analysis tools to accomplish this complex task.

The biggest limitation in classic structural design is the use of very simple components as straight spars and ribs, quadrilateral panels, uniform-thickness stiffeners, and stringers. Moreover, all these structural elements have to be connected using bolts and rivets or by welding, which are time- and money-consuming processes. Thus, the trend in the industry is toward designing structures with fewer components, but more efficiently. This philosophy leads to the development of the so-called *unitized structures*, characterized by the integration of the stiffening members to the rest of the structure achieving a monolithic construction of the vehicle [1]. The advantages of the use of unitized structure [2] over classical designed structures are multiple and can be identified as follows: 1) reduced part count, manufacturing time, and fabrication cost; 2) increased design flexibility; 3) weight savings; 4) increased resistance to fatigue and corrosion; 5) enhanced automation; and 6) improved ergonomics and reduced work.

The benefits of unitized structures are so overpowering that experts expect an exponential increase in the use of this kind of structure in the aeronautics and aerospace design by 2020 [1]. Major aircraft manufacturer companies lead this revolution in structural design approach. In particular, Boeing already has developed a new integrally stiffened fuselage concept whose testing demonstrated structural performance and efficiency similar to those of conventional design, while achieving significant manufacturing time and cost reduction [3]. The manufacturing of unitized structures is directly linked to the development of new innovative manufacturing techniques as rapid manufacturing, rapid prototyping, solid free-form fabrication, and additive manufacturing [4,5]. Friction stir welding [6] and electron beam free-form fabrication (EBF^3) [7–9] are among the most promising manufacturing techniques that can be used to produce metallic unitized structures for the aeronautics industry. Furthermore, these techniques enable the manufacturing of integrated curvilinear stiffening members with negligible additional cost and time with respect to conventional processes. This aspect is crucial for the optimization of the airframe components, since

Presented at the 51st AIAA/ASME/ASCE/AHS/ASC Structures, Structural Dynamics and Material Conference, Orlando, FL, 10–15 April 2010; received 8 December 2010; revision received 18 April 2011; accepted for publication 19 April 2011. Copyright © 2011 by Davide Locatelli, Sameer B. Mulani, and Rakesh K. Kapania. Published by the American Institute of Aeronautics and Astronautics, Inc., with permission. Copies of this paper may be made for personal or internal use, on condition that the copier pay the \$10.00 per-copy fee to the Copyright Clearance Center, Inc., 222 Rosewood Drive, Danvers, MA 01923; include the code 0021-8669/11 and \$10.00 in correspondence with the CCC.

*Research Assistant, Engineering Science and Mechanics. Student Member AIAA.

†Postdoctoral Fellow, Aerospace and Ocean Engineering. Senior Member AIAA.

‡Mitchell Professor, Aerospace and Ocean Engineering. Associate Fellow AIAA.

topology optimization methods lead often to curved designs [10]. The use of curved stiffening members broadens the design space and provides variable stiffness, enabling a more efficient structural and material tailoring. The concept of variable stiffness is not new in aeronautical design. In fact, nonuniformly stiffened structures have been used in the construction of airframes since the dawn of aerospace history. Straight stiffeners are commonly used to provide panels with additional stiffness along the direction of the acting loads [11]. Moreover, the stiffeners can be placed at different orientations to align with the stress flow in the structure and to provide an efficient load-bearing mechanism. Use of multiple stiffeners is also advantageous, since it provides redundancy and efficiently stops the growth of cracks in the supporting substructure [11]. A further improvement in airframe panel design is represented by the introduction of geodesically stiffened panels, whose optimization and structural response was widely studied by Gürdal and Gendron [12], Gürdal and Grall [13], Gendron and Gürdal [14], and Grall and Gürdal [15]. Isogrid [16] and grid-stiffened [17,18] panels are also commonly used in aircraft design for their efficiency in load-carrying capability and buckling behavior [19].

The broad use of composite materials is also motivated by the need for nonuniformly stiffened structures. Hence, the composites have always been an integral part of aircraft structural layout, from the wood ply composite materials introduced in the 1920s [20] to the most advanced nonuniformly distributed curved fibers and matrix composites used for differential stiffening of fuselage structures [21].

The variable-stiffness approach is also applied globally to the construction of the complete wing structure. Generally, in this case, the stiffness of the wing is controlled using actuators. Studies from Chen et al. [22] and Onoda et al. [23], have shown the advantage of variable-stiffness spars and trusses in improving the flight quality, controlling the vibrations, and providing stress relief to the structure. However, the use of actuators to modify the stiffness can lead to increased structural weight and complicated design solutions for the actuator-structure integration. Hence, the use of curvilinear spars and ribs or *SpaRibs* (see Fig. 1) can combine the advantages of the variable-stiffness design concept while avoiding the problems of the use of actuators. Furthermore, these two approaches are fundamentally different; the first approach falls under the active structure control category and its purpose is to ameliorate the structural performance at certain flight conditions; on the other hand, the *SpaRibs* provide passive control of the structure and aim to improve the performance across the whole flight envelope. Kobayashi et al. [24,25] and Kolonay and Kobayashi [26] have shown how curvilinear internal structures resulting from the topology optimization using the cellular-division approach are beneficial for the multidisciplinary optimization of air vehicles.

Curved beams behave very differently from conventional straight beams used for the structural layout of wing boxes. Love [27] demonstrated that both axial and torsional deformations are coupled with bending for curved beams of arbitrary shape and derived the governing equations. The advantages of using *SpaRibs* in the wing-box layout reside exactly in the coupling between bending and

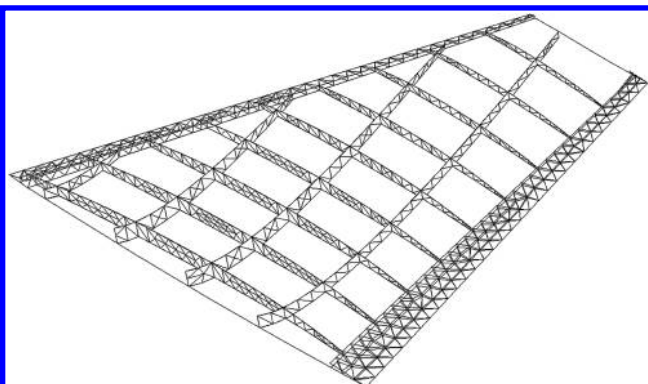


Fig. 1 Supersonic wing internal structure FE model showing the use of curvilinear spars and ribs or *SpaRibs* to improve the design.

torsion that characterizes curved beams and can be described as follows:

1) Torsional deformation of the wing due to the aerodynamic loads can be counteracted by suitably placing *SpaRibs* with the additional effect of relieving the shear stresses in the skin panels by reducing the torsional deformation itself.

2) Natural frequencies and mode shapes can be controlled.

3) Structural coupling between bending and torsion can be exploited to passively control the flutter mechanism.

4) Increased stiffness achieved with *SpaRibs* allows design airfoil cross sections to be designed with reduced thickness-to-chord ratio, decreasing the drag and the boom signature.

5) There is reduced airframe weight for the same performance.

In conclusion, the introduction of unitized structures concept, the availability of innovative manufacturing techniques such as EBF³, and the curved designs resulting from topology optimization require the development of tools that are able to analyze and optimize airframes with curvilinear *SpaRibs*.

The problem approached by this research is the optimization of a wing-box-like structure using curvilinear *SpaRibs* instead of using the classic design concept of straight spars and ribs. In particular, the minimum-weight design has been studied under stress and buckling constraints. The external shape of the wing box is fixed and the aerodynamic loads used in the study cases are simple estimates of the real flight loads. The internal structure is placed by EBF3SSWingOpt according to the design-variable vector, and the structural analysis is performed by MD Nastran. Finally, the weight of the optimized structure is compared with the weight of a baseline structure with straight internal elements to study the potential advantage of the use of the *SpaRibs* in fabricating lighter aircraft structures.

Section II describes in detail the framework developed for the optimization. In particular, a *one-step* approach and a *two-step* approach to the optimization are presented. In Sec. III the parameterization of the *SpaRibs* is described. Section IV shows the formulation of the optimization problem. In particular, the formulation of the response functions is stated and a list of design variables is given. Section V presents the results of the application of the optimization framework. At first, a parametric study is performed to characterize the behavior of the response functions in the design space. Subsequently, the optimization using *SpaRibs* is applied to a rectangular wing box. Finally, the process is used to optimize a generic fighter wing structure. The one-step and two-step optimization performances are also compared.

II. Global Optimization Framework

The methodology developed to carry out the weight optimization of any aerospace structure has to take into account all the different aspects and disciplines involved in the design, such as stresses in the structure, buckling phenomena, vibrational modes interaction, aerodynamics and structure interaction, thermal loads, and robustness of the design and reliability (see Fig. 2). This study focuses only on static stress analysis and buckling, excluding the rest of the disciplines from the optimization process. A multidisciplinary optimization framework that involves topology optimization requires the capability to update the geometry and finite element (FE) model at every iteration. Hence, the following steps define the general optimization algorithm for the single iteration:

1) The optimizer checks convergence of the design and eventually computes a new design-variable (DV) vector.

2) Geometry and structural FE model are updated accordingly to the new DV vector.

3) Structural static and buckling analyses of the updated FE model are performed.

4) FE analysis results are retrieved and response functions are built.

5) Response functions are fed back to the optimizer.

To accomplish these tasks, a framework capable of linking and coordinating different commercially available software has been developed. In Fig. 3, the global schema is presented; the MATLAB-based [28] EBF3SSWingOpt code is used to link together the

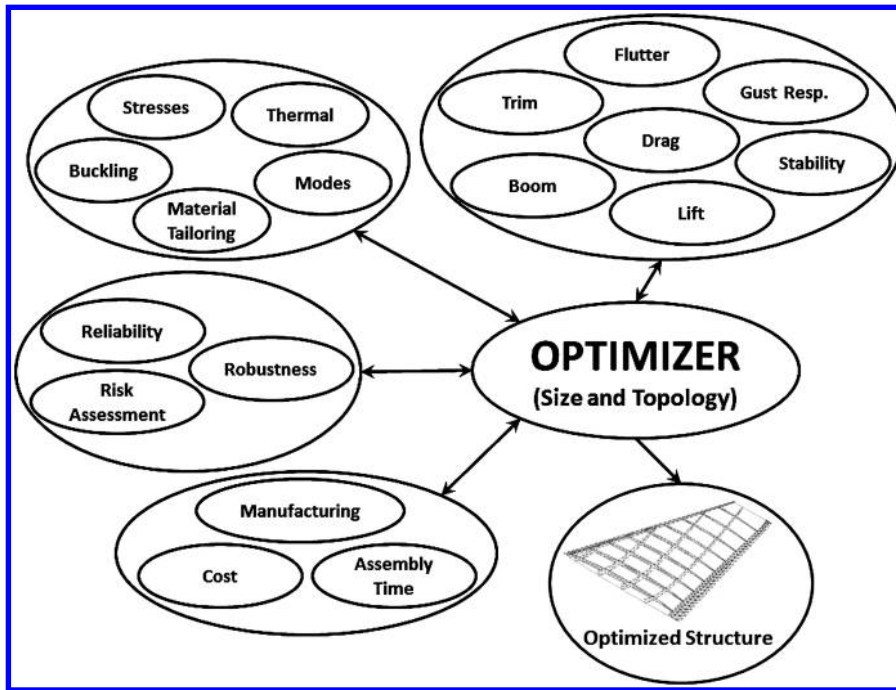


Fig. 2 General multidisciplinary design optimization scheme. The optimizer receives the responses from various disciplines and subdisciplines and computes the optimum topology and size of the structure. The SpaRibs enlarge the design space size.

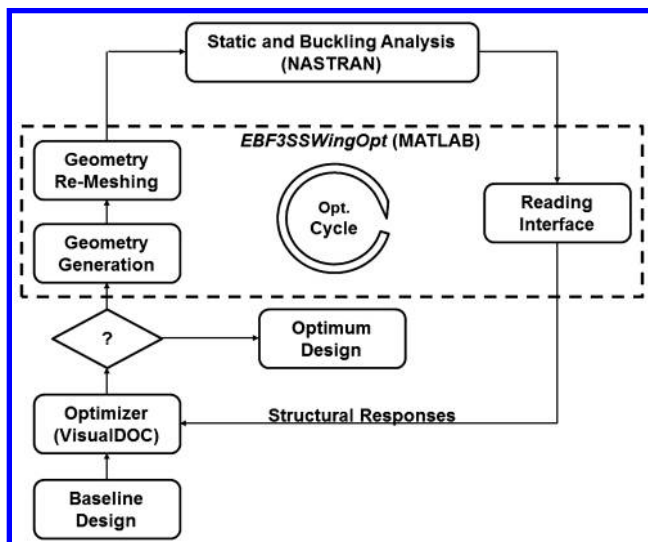


Fig. 3 Block diagram of the optimization scheme; the dashed line encloses the functionalities of EBF3SSWingOpt.

optimizer, VisualDOC [29], and the analysis software. The user sets the optimization problem by building a VisualDOC database (including the objective and constraints functions, the DV vector and the side constraints, and the starting design point) and by selecting the most suitable optimization method to use: namely, the gradient-based methods, the response-surface-based methods, the genetic algorithm (GA) method, and the particle swarm optimization (PSO) method. Once the VisualDOC database is correctly completed, an optimization task is launched by the user via MATLAB; from this moment on, the optimization is completely automatic and does not require any additional input from the user. The automatic process starts with VisualDOC supplying the DV vector to EBF3SSWingOpt, which uses these data to generate an MD Patran [30] input session file; MD Patran reads the input session file and generates the geometry, the mesh, and the MD Nastran [31] input file. This process ensures the consistency between the geometry and the mesh for the computation of the right responses. MD Nastran performs static stress analysis, buckling, and modal analyses of the structure and

writes all the results in an output file that is scanned by EBF3SSWingOpt to retrieve the objective functions values, for the design point considered, and feeds them back to VisualDOC. If the objective function is converged and the constraints functions are satisfied, the optimization is completed and a file including the best design and the history of the optimization DV vector and response functions is printed out; otherwise, VisualDOC provides EBF3SSWingOpt with a new DV vector and the cycle starts again. There are cases where the analysis cannot be completed for different reasons, the most common of which is the failure to build a correct mesh by MD Patran on very complex geometries. In these cases, it is impossible to retrieve the values of the response functions; hence, the particular design point is automatically excluded from the optimization and a warning message is printed out in the results file.

A global optimization framework, such as the one we have developed thus far, includes two main optimization problems; the sizing optimization of each structural component and the topology optimization of the structure. The topology optimization addresses issues such as how many components and what shape they must have to reach the best design. Obviously, sizing and topology optimization are coupled together; in other words, changing the size of the components of the structure leads also to a change in the topology and vice versa. Therefore, the complexity of this problem is greater than the complexity of a simple sizing optimization problem. However, optimizing both the size and the topology of the structure is of enormous advantage to the designer, since that provides a much wider design space and multiple design solutions that are equally advantageous with respect to the weight reduction, but that differ from each other in terms of the stresses and deformations distribution or the buckling behavior or the mode shapes and natural frequencies.

The natural approach to solve the problem is to address sizing and topology optimization at the same time and to solve the coupled problem, using what we called *one-step optimization* [32]. However, in an attempt to improve the efficiency of our framework, we also developed a *two-step optimization* [33–35], in which the two problems are solved in an uncoupled but an iterative manner. These two methodologies are described in the following.

A. One-Step Optimization

In the one-step optimization methodology, both the size and the topology optimization problems are solved as one problem in each

Table 1 One-step optimization response functions

Response ^a	Description
Objective function	Minimum W , lb
Constraint	$BF_0 < 1$
Constraint	$KSC_\sigma < 1$

^aThe objective function is the weight of the structure; the constraints are the buckling factor and the KS coefficient for the von Mises stresses.

iteration according to the general scheme presented in Fig. 3. The weight of the structure is minimized subject to the stress and buckling constraints, as shown in Table 1. Performing an optimization using this method can require extensive CPU time, due to the large number of design variables; however, it has the advantage that the user has to build just one VisualDOC database and there is no need to iterate between sizing and shape optimization to achieve the convergence of the objective function.

B. Two-Step Optimization

In the two-step optimization methodology, the size and the topology optimization problems are solved as uncoupled problems in two different steps in which the objective function is chosen properly and does not have to be the same for the sizing and the topology problems. For an optimization problem, where the weight, the buckling factor, and the stresses are considered as response functions, the two-step optimization scheme is presented in Fig. 4. The DV vector is split into two vectors: one vector consists of all the DVs related to the sizing problem and the other vector is where all the DVs related to the topology problem are grouped. The user has to make a choice of which design variable belongs to which problem based on his/her experience and judgment. Two VisualDOC database are created: one for optimizing the size of the elements and one for optimizing their topology. At this point, it is clear that the FE model must be regenerated only for the topology step of the optimization, which works exactly following the scheme in Fig. 3, with the advantage that now the DVs are less in number than if the coupled problem was solved, achieving a faster convergence to the optimum solution of the topology problem. Since the sizing step of the optimization does not require that the FE model is updated at every

Table 2 Two-step optimization response functions description for the topology optimization

Response	Description
Objective function	Minimum BF_0
Constraint	$W/W_{MAX} \leq 1$
Constraint	$KSC_\sigma < 1$

Table 3 Two-step optimization response functions description for the size optimization

Response	Description
Objective function	Minimum W , lb
Constraint	$BF_0 < 1$
Constraint	$\sigma_{VM}/\sigma_y < 1$

iteration, EBF3SSWingOpt can be used only to update the thicknesses of the structural components, without the need to go through the geometry generation and the geometry remeshing phases, therefore also greatly improving the efficiency for this step. The disadvantage of this method is that to achieve the global convergence of the optimum design, these two steps have to be executed iteratively. However, convergence is usually obtained after two or three iterations of each step. Results will be presented in Sec. V, which will show the comparison of the achievements obtained using these two methodologies and will prove that the two-step optimization is slightly more efficient than the one-step optimization.

It is important to emphasize that the optimization problems related to each step have to be carefully formulated to reach a feasible optimum design. Tables 2 and 3 show the appropriate formulation used to solve an optimization where the weight, the buckling factor, and the stresses are used as responses.

In the topology optimization step, the optimizer looks for the stiffest configuration possible, whereas the weight and the stresses cannot exceed a given value, and the thicknesses of each component of the structure are constant. Instead, in the size optimization step, the optimizer looks for the lightest configuration possible, whereas the

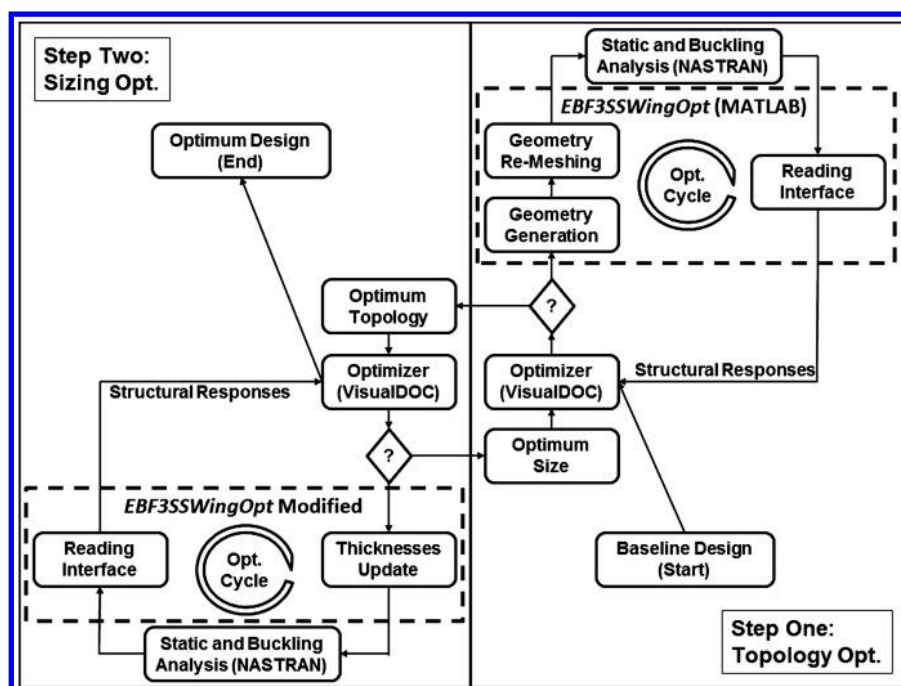


Fig. 4 Two-step optimization block diagram. The optimization starts with the baseline design. The first step is the topology optimization that follows the global scheme presented in Fig. 3. Once the best topology is computed, the design is fed to the second step. In the sizing phase, the thickness of each component is optimized without changing the shape of the structure. The two steps can be iterated until convergence of the design is reached.

buckling factor has to be smaller than 1, the von Mises stresses is lower than the yield stress of the material, and the topology of the structure is fixed.

III. Wing Parametric Geometry Generation

In Sec. II, the general optimization approach was presented. It is important to understand that the global schema is applicable to any type of structure and, in principle, could include any type of response functions and constraints provided by specific disciplines related to the design. In the following section, the application of the global schema to the design of winglike structures is described. The peculiarity of these kinds of structures is the use of three types of components that are different for their design and load-carrying functions. The components are the skin panels, the spars, and the ribs. To carry out an optimization process that involves topology optimization, a geometry parameterization of the structural components is needed. The parameters chosen to describe the geometry of the structural elements will be used as topology-related DVs.

There are multiple equivalent ways to parameterize the geometry of the structure according to different user requirements. In this case, the wing planform and the airfoil cross section are fixed during the optimization, whereas the shape of spars and ribs is changing; hence,

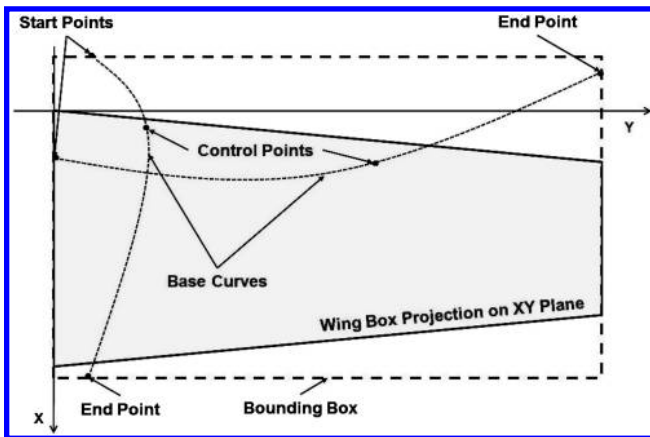


Fig. 5 Geometry parameterization using B-splines and the concepts of base curves and bounding box. The base curves are modeled as third-order B-splines. The start- and endpoints of the curves are constrained to lay on two opposite edges of the bounding box. The control points lay within the bounding box.

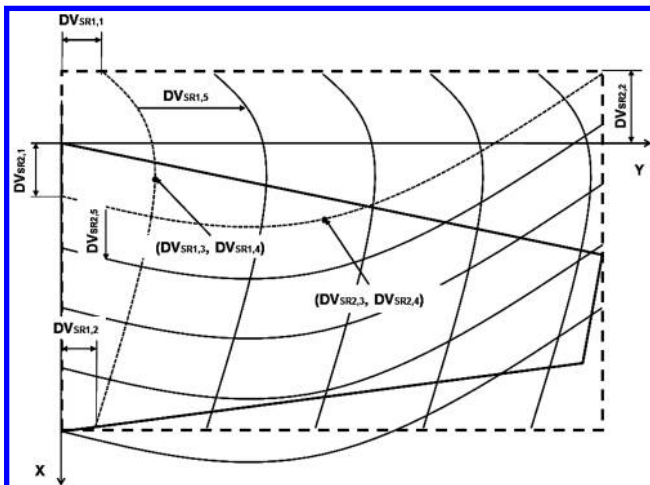


Fig. 6 Topology DVs for SpaRibs shape and placing optimization. $DV_{SR1,1}$ is the Y coordinate of the start point of the first base curve; $DV_{SR1,2}$ is the Y coordinate of the endpoint; $DV_{SR1,3}$ and $DV_{SR1,4}$ are the X and Y coordinates of the control point, respectively; $DV_{SR1,5}$ is the distance between two SpaRibs. $DV_{SR2,1}$, $DV_{SR2,2}$, $DV_{SR2,3}$, $DV_{SR2,4}$, and $DV_{SR2,5}$ have similar significance, but they refer to the second base curve.

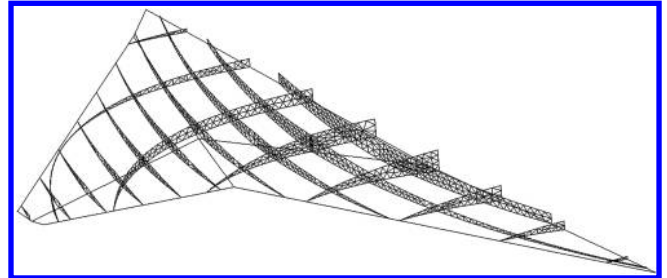


Fig. 7 Wing mesh generated by EBF3SSWingOpt using base curves and bounding-box method to parameterize the SpaRibs geometry.

for our purposes, only the parameterization of the internal structural components was needed. Our choice was mainly dictated by how the geometry is generated in MD Patran; as a consequence, it was natural to choose the B-spline utility of MD Patran to parameterize the shape of the SpaRibs. Figure 5 shows how the SpaRibs are generated using B-splines and the concepts of *base curves* and *bounding box* [36].

Base curves are generated interpolating three points, indicated in Fig. 5, as the start point, the control point, and the endpoint, with MD Patran B-spline utility. The start- and endpoints of each base curve are always located on two opposite edges of the bounding box, a rectangle whose dimensions are constant and provided by the user, enclosing the projection of the wing planform on the X–Y plane. The SpaRibs are then generated translating each of the base curves in X and Y directions, respectively, as displayed in Fig. 6.

This formulation allows the reduction from six to four parameters to describe each base curve. To generate a B-spline curve, the user should provide the coordinates of the start, the control, and the endpoints corresponding to six geometric parameters for a single curve. In Fig. 7, we present an example of a wing for which the geometry was generated as described above.

IV. Optimization-Problem Formulation

The optimization-problem statement is described mathematically by Eq. (1), where $f(\mathbf{x})$ is the objective function, $g_i(\mathbf{x})$ are the n response constraints, $x_{j\min}$ and $x_{j\max}$ are the side constraints for each of the m DVs, and \mathbf{x} is the DV vector:

$$\begin{aligned} \min_{\mathbf{x}} f(\mathbf{x}) \quad & g_i(\mathbf{x}) \leq 1 \quad i = 1, \dots, n \\ x_{j\min} \leq x_j \leq x_{j\max} \quad & j = 1, \dots, m \end{aligned} \quad (1)$$

The response functions and each DV are supposed to be continuous in the space enclosed by their related constraints.

A. Response Functions

The response functions are defined by the values assumed by the variables calculated at each step of the analysis. The same response function can be characterized as objective function, as constraint function, or both, depending on the formulation of the optimization problem. In this particular case, the response functions are related to structural parameters that define the general performance of the structure and are defined as follows: wing weight W , wing buckling factor BF_0 , Kreisselmeier–Steinhauser stress coefficient KSC_σ , and maximum von Mises stress σ_{VM} .

These response functions can be used as objectives or as constraints, depending upon the problem statement, as described in Tables 1–3.

Although the weight of the structure, W , is directly given in the MD Nastran analysis output file, the rest of the response functions have to be computed using data contained in the same result file.

The wing buckling factor BF_0 is calculated according to Eq. (2):

$$BF_0 = \frac{1}{\lambda_0} \quad (2)$$

The fundamental buckling eigenvalue λ_0 is obtained from the SOL 105 sequence in MD Nastran and defines the static instability

behavior of the structure. The critical buckling load P_{cr} is defined in Eq. (3), where P is the applied load:

$$P_{cr} = \lambda_0 P \quad (3)$$

It is clear that if $\lambda_0 \geq 1$, then $P_{cr} \geq P$, meaning that the structure is statically stable under the applied load system. Hence, the mathematical formulation of the buckling constraint can be written as in Eqs. (4) and (5). Note that in Eq. (5), a safety factor (SF) has been taken into account:

$$\frac{1}{\lambda_0} \leq 1 \quad (4)$$

$$\frac{SF}{\lambda_0} \leq 1 \quad (5)$$

The Kreisselmeier–Steinhauser [37] stress coefficient KSC_σ defines an aggregated von Mises stress parameter for all elements in the FE model and is computed using Eq. (6):

$$KSC_\sigma(\sigma) = \frac{1}{\rho} \ln \left(\frac{1}{\sum_{i=1}^N A_i} \sum_{i=1}^N e^{\rho \frac{\sigma_i}{\sigma_y}} \right) \quad (6)$$

Here, A_i is the area of the i th element, σ_i is the von Mises stress in the i th element, σ_y is the yield stress of the material, and ρ is a constant whose value determines the behavior of the constraint. A low value of ρ tends to average the stresses smoothing the constraint; on the contrary, a high value of ρ drives the constraint to its maximum value. In this case, a rather high value of 150 was used for ρ .

The maximum von Mises stress is calculated as

$$\sigma_{VM} = \max_i(\sigma_i) \quad (7)$$

Note that σ_i is the von Mises stress computed by MD Nastran in the i th finite element. If the maximum von Mises stress σ_{VM} is smaller than the material yield stress σ_y , then the static stress constraint is met and can be formulated as in Eqs. (8) and (9), whereas in Eq. (9), a safety factor has been introduced:

$$\frac{\sigma_{VM}}{\sigma_y} \leq 1 \quad (8)$$

$$\frac{\sigma_{VM} SF}{\sigma_y} \leq 1 \quad (9)$$

B. Design Variables

The type and the number of design variables of the optimization are directly related to the parameterization of the geometry of the

structure. With the current parameterization method, described in Sec. III and presented in Fig. 6, a total of 10 design variables are needed to allow the topology of the SpaRibs to change. At least another four design variables are needed for the thicknesses of the structure. Table 4 details these 14 design variables used to solve this optimization problem. The side constraints for the sizing variables are given by the manufacturing capabilities. The minimum thickness value is an important constraint, since the thinner the structure is, the better it is from a weight point of view. The SpaRibs control-point coordinates are limited by the dimensions of the bounding box [36], and the design variables that define the distance between two SpaRibs have to be greater than zero.

V. Results

In this section, results for two cases are presented. The first case is a rectangular wing box that is optimized using bigrid and curvilinear SpaRibs, respectively. The second case is a generic supersonic fighter wing optimized using curvilinear SpaRibs. Particle swarm optimization [36,38,39] is used to carry out the optimization analysis. This method was chosen to avoid, as much as possible, local minima regions in the design space.

A. Rectangular Wing Box

This case was chosen as a test case to evaluate the aforementioned optimization framework and to prove the advantage of using curvilinear SpaRibs for designing wing structures. The wing box is a rectangular with constant thickness of 0.8 in., a semispan of 15 in., and an airfoil chord of 30 in.

The baseline wing was provided by Lockheed Martin Aeronautics Company and is characterized by an internal structure with six spars and two ribs (Fig. 8). The material is aluminum alloy 2124-T851, for which the properties are given in Table 5.

A pressure distribution linearly varying over the chord length, also provided by Lockheed Martin Aeronautics Company, is used as the load case. At the leading edge ($x = 0$ in.), $P = 2.027$ psi. At the trailing edge ($x = 30$ in.), $P = 4.480$ psi. A parametric study was performed before proceeding to the optimization to have an idea of the variation of the response functions. The weight, buckling factor, and Kreisselmeier–Steinhauser stress coefficient were computed for the rectangular wing with straight spars and ribs. The value of the distance between two spars was changed for each analysis, whereas the rest of the values of the DVs were kept constant (see Table 6).

In Figs. 9–11, we present the results of the parametric study. The weight W response seems to be well-behaved, as compared with the BF_0 and the KSC_σ responses. As the distance between the spars increases, the weight of the wing decreases, since fewer and fewer spars are included in the wing box. The steplike trend of the weight response is due to the fact that increasing the distance pushes the spars out of the wing box one at a time. Each step in the function corresponds to the change in the number of spars in the wing. The behaviors of the BF_0 and the KSC_σ responses are more erratic, with a large number of peaks and valleys, although the general trend of both functions is to increase their values as the distance increases.

Table 4 Optimization design variables

Design variable	Description
Upper-skin thickness, in.	Sizing variable
Lower-skin thickness, in.	Sizing variable
Spar thickness, in.	Sizing variable
Rib thickness, in.	Sizing variable
Spar start-point x coordinate, in.	Topology variable
Spar control-point x coordinate, in.	Topology variable
Spar control-point y coordinate, in.	Topology variable
Spar endpoint x coordinate, in.	Topology variable
Spar distance, in.	Topology variable
Rib start-point y coordinate, in.	Topology variable
Rib control-point x coordinate, in.	Topology variable
Rib control-point y coordinate, in.	Topology variable
Rib endpoint y coordinate, in.	Topology variable
Rib distance, in.	Topology variable

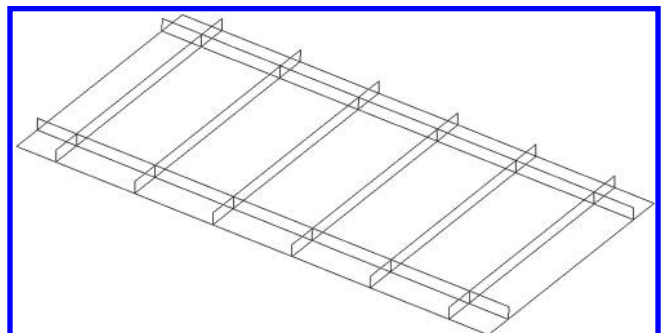


Fig. 8 Baseline rectangular wing-box geometry. The internal structure counts six straight spars and two straight ribs.

Table 5 Aluminum alloy 2124 T851 mechanical properties

Property	Value
Young's modulus E	10.6 Msi
Poisson's ratio ν	0.33
Density σ	0.101 lb/in. ³
Yield stress σ_y	64 ksi
Ultimate tension stress σ_u	70 ksi

Table 6 Values assumed by the design variables during the parametric study^a

Design variable	Value
Upper-skin thickness, in.	0.2 (fixed)
Lower-skin thickness, in.	0.2 (fixed)
Spar thickness, in.	0.2 (fixed)
Rib thickness, in.	0.2 (fixed)
Spar start-point x coordinate, in.	2.5 (fixed)
Spar control-point x coordinate, in.	2.5 (fixed)
Spar control-point y coordinate, in.	7.5 (fixed)
Spar endpoint x coordinate, in.	2.5 (fixed)
Spar distance, in.	Changing
Rib start-point y coordinate, in.	1.85 (fixed)
Rib control-point x coordinate, in.	15 (fixed)
Rib control-point y coordinate, in.	1.85 (fixed)
Rib endpoint y coordinate, in.	1.85 (fixed)
Rib distance, in.	11.3

^aAll variables are constant except for the distance between the spars.

A similar study was done changing the orientation of the spars and keeping the rest of the DVs constant, showing similar discontinuous behavior of the responses. Therefore, we can conclude that the response functions for this particular problem are very sensitive to small changes in the topology DVs; in particular, the BF_0 and the KSC_σ functions display this kind of behavior. This could generate problems for the optimizer, especially if gradient-based methods or sensitivity-based methods are used to evaluate the response functions.

1. Rectangular Wing Box with Bigrid

Before approaching the more complex problem of optimizing the structure using SpaRibs, we solved a much simpler problem of optimizing the rectangular wing box with a bigridlike internal configuration. With this approach, the spars and ribs are considered

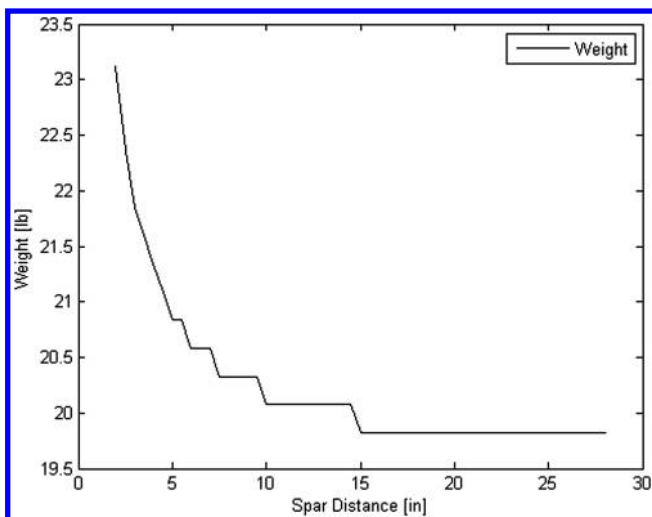


Fig. 9 Wing weight variation for changing in the distance between spars.

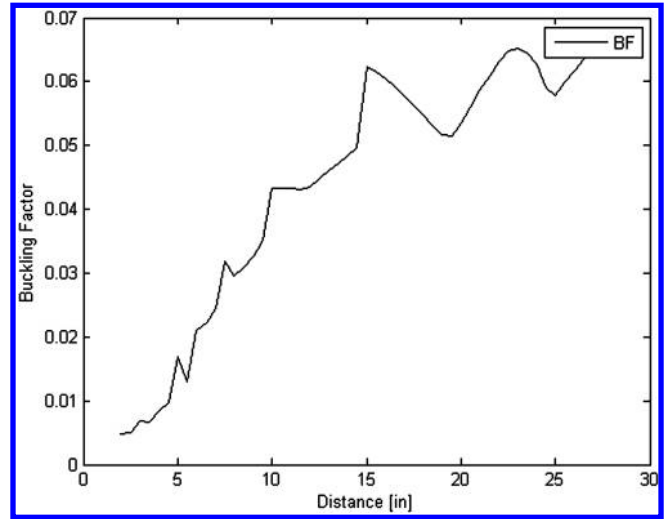


Fig. 10 Wing buckling-factor variation for changing in the distance between spars.

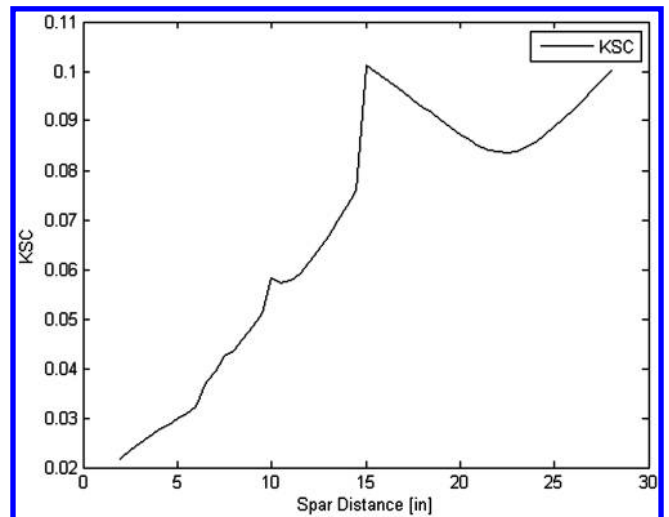


Fig. 11 Wing Kreisselmeier-Steinhauser stress coefficient variation for changing in the distance between spars.

as straight structures with fixed orientation, and they are orthogonal to each other. The geometry update and remeshing of the FE model are less complex than for the case of curvilinear spars and ribs. This problem can be seen as the optimization problem described in Sec. IV, but with a reduced number of DVs. Indeed, only the thicknesses of the structural elements and the distances between spars and ribs are changed, whereas the rest of the DVs are kept constant.

Two different sets of results are presented below. The first set refers to a configuration where the spars and ribs are uniformly distributed; in other words, the distance between any two spars next to each other

Table 7 Bigrid optimization of the rectangular wing box using uniformly spaced spars and ribs^a

No. ribs	No. spars								
	2	3	4	5	6	7	8	10	12
2	5.61	5.13	4.44	4.12	4.03	4.06	3.82	3.54	3.43 ^b
3	5.56	5.01	4.35	4.35	4.16	3.96	3.95	3.61	3.48
4	5.24	4.61	4.58	4.47	4.26	4.11	3.93	3.78	3.77

^aThe weight of the structure is optimized for configurations with different numbers of spars and ribs. The best results are obtained with 12 spars and two ribs. The weight is in pounds.

^bIndicates the lighter structure.

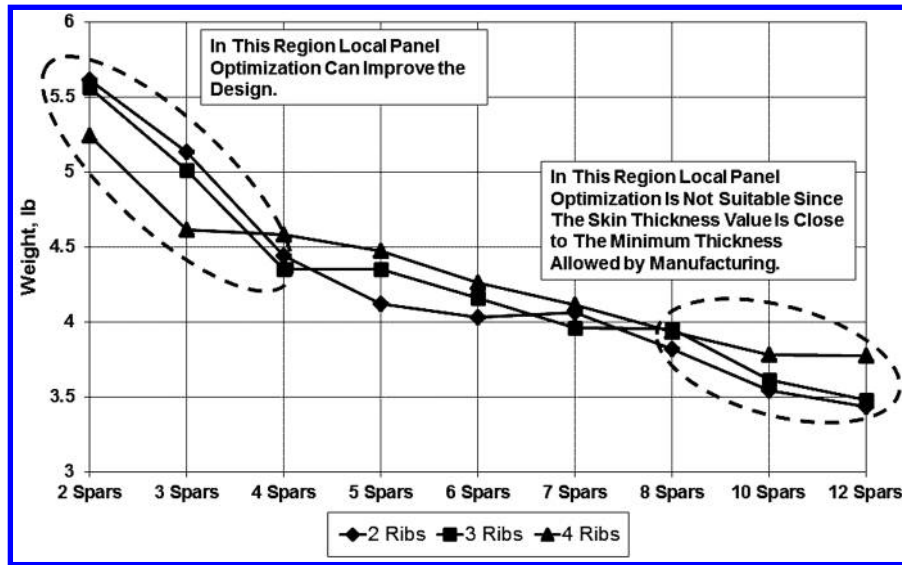


Fig. 12 Weight optimization of rectangular wing box using uniformly spaced bigrid.

is the same. The results are visualized in Table 7 and in Fig. 12. The second set of results refers to a configuration where the spars and ribs are nonuniformly distributed. An additional DV is introduced to define a nonuniform spacing; see Table 8 and Fig. 13 for the detailed results.

For the uniformly distributed spars and ribs problem, the optimum result is obtained for the configuration with 12 spars and two ribs, as opposed to the optimum configuration with 12 spars and three ribs obtained with nonuniform distribution. As shown in Figs. 12 and 13, configurations with less spars and ribs are worse in terms of the

weight. However, if the number of spars and ribs is fixed by the designer, it is possible to improve these designs, proceeding to a local panel optimization, as described in Mulani et al. [36]. A description of a collaborative global–local optimization is beyond the scope of this paper; nevertheless, it is possible to combine the two aspects to improve the structure performance.

The designs with a large number of spars and ribs are more advantageous. The explanation of this phenomenon is related to the driving constraint of the optimization problem. Analyzing the results of several optimization cycles, we noticed that the driving constraint is always the BF_0 . In other words, the wing will fail because the buckling constraint is violated long before the stress constraint becomes active. This means that if we want to improve the design, we need to improve the buckling properties of the structure. Ultimately, the global static instability is due to the buckling of the skin local panels; therefore, if the load is fixed, it is possible to design stiffer yet thinner panels, thus reducing their dimensions. Adding spars and ribs produces exactly this effect on the structure. The local panels are smaller; hence, they can sustain the same load without buckling and with reduced thickness. This process is a tradeoff between the weight gained because of the additional spars and ribs and the weight lost because of the decreased skin thickness. When the optimum configuration of spars and ribs is reached, increasing the number of internal elements becomes disadvantageous, since the weight gain

Table 8 Bigrid optimization of the rectangular wing box using nonuniformly spaced spars and ribs^a

No. ribs	No. spars								
	2	3	4	5	6	7	8	10	12
2	5.79	4.95	4.59	4.20	3.86	3.73	3.57	3.45	3.60
3	5.16	4.49	4.50	3.97	3.90	3.78	3.75	3.58	3.34 ^b
4	4.95	4.22	3.83	3.60	3.66	3.53	3.58	3.39	3.47

^aThe weight of the structure is optimized for configurations with different numbers of spars and ribs. The best results are obtained with 12 spars and three ribs. The weight is in pounds.

^bIndicates the lighter structure.

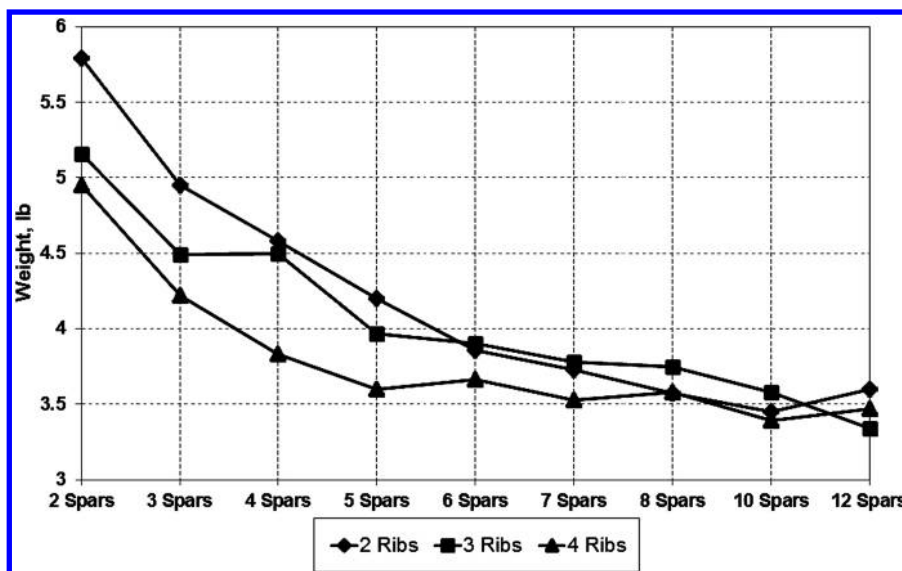


Fig. 13 Weight optimization of rectangular wing box using nonuniformly spaced bigrid.

Table 9 Optimal design thicknesses for the rectangular wing

	Uniform distribution	Nonuniform distribution	Baseline
Upper-skin thickness, in.	0.015	0.032	0.06
Lower-skin thickness, in.	0.015	0.015	0.06
Spar thickness, in.	0.036	0.015	0.04
Rib thickness, in.	0.015	0.015	0.04

due to the added structural component is not compensated by the weight reduction due to the reduced skin thickness, leading to an overall weight increase.

In Table 9, the thickness of the structure is shown for both optimum bigrid configurations found. The minimum manufacturing thickness of 0.015 in. is reached in almost every part of the skin.

2. Rectangular Wing Box with Curvilinear SpaRibs

The optimization of the rectangular wing box using uniformly and nonuniformly spaced bigrid is the first step toward the implementation of curvilinear SpaRibs. In this section, three sets of optimization results with SpaRibs are presented. The first two sets are

Table 10 DV results for the rectangular wing optimized using curvilinear SpaRibs and one-step optimization framework: case I

Design variable	Optimized	Baseline
Upper-skin thickness, in.	0.038	0.06
Lower-skin thickness, in.	0.040	0.06
Spar thickness, in.	0.015	0.04
Rib thickness, in.	0.015	0.04
Spar start-point x coordinate, in.	1.871	2.5
Spar control-point x coordinate, in.	0.142	2.5
Spar control-point y coordinate, in.	3.519	7.5
Spar endpoint x coordinate, in.	-2.000	2.5
Spar distance, in.	4.2065	5.0
Rib start-point y coordinate, in.	-0.870	1.85
Rib control-point x coordinate, in.	21.331	15.0
Rib control-point y coordinate, in.	1.026	1.85
Rib endpoint y coordinate, in.	-1.545	1.85
Rib distance, in.	2.000	11.3
Responses		
W , lb	4.62	5.91
BF_0	0.699	0.587
KSC_σ	0.284	N/A

Table 11 DV results for the rectangular wing optimized using curvilinear SpaRibs and one-step optimization framework: case II

Design variable	Optimized	Baseline
Upper-skin thickness, in.	0.034	0.06
Lower-skin thickness, in.	0.037	0.06
Spar thickness, in.	0.019	0.04
Rib thickness, in.	0.015	0.04
Spar start-point x coordinate, in.	5.000	2.5
Spar control-point x coordinate, in.	1.500	2.5
Spar control-point y coordinate, in.	5.434	7.5
Spar endpoint x coordinate, in.	4.612	2.5
Spar distance, in.	2.500	5.0
Rib start-point y coordinate, in.	3.422	1.85
Rib control-point x coordinate, in.	12.000	15.0
Rib control-point y coordinate, in.	3.579	1.85
Rib endpoint y coordinate, in.	12.500	1.85
Rib distance, in.	5.478	11.3
Responses		
W , lb	4.19	5.91
BF_0	0.752	0.587
KSC_σ	0.284	N/A

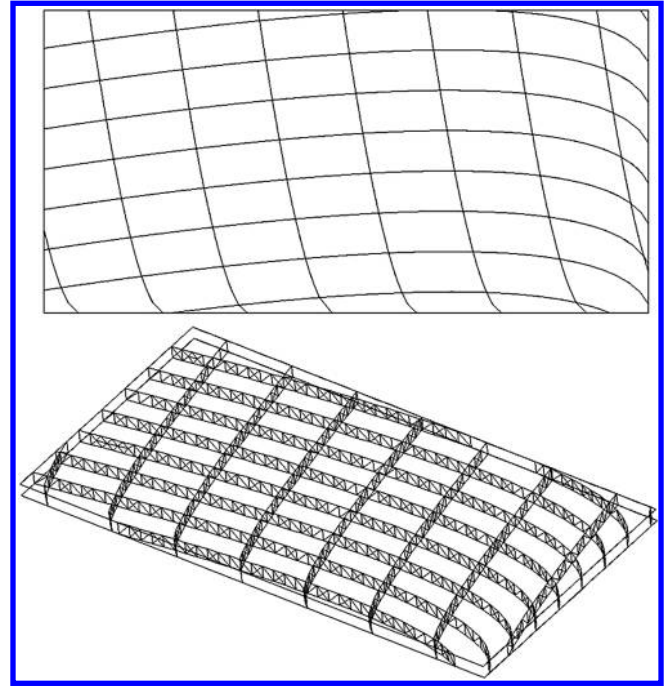


Fig. 14 Internal structure of rectangular wing optimized using curvilinear SpaRibs and one-step optimization: case I.

obtained with the one-step optimization framework, and the third set is obtained by applying the two-step optimization framework.

In Tables 10 and 11, we present the DV vectors of the optimum configurations found using the one-step optimization framework presented in Sec. II. These result are obtained with PSO optimization method with a population size of five particles. The starting design point and some of the side constraints characterizing the boundaries of the DVs are different and account for the different optimum designs reached.

Figures 14 and 15 show the internal topology of the optimized rectangular wing box. The two topologies are completely different from one another and yet their weights are in the same range. The advantage of having such different structures with similar buckling and weight properties is clear if we consider the fact that the

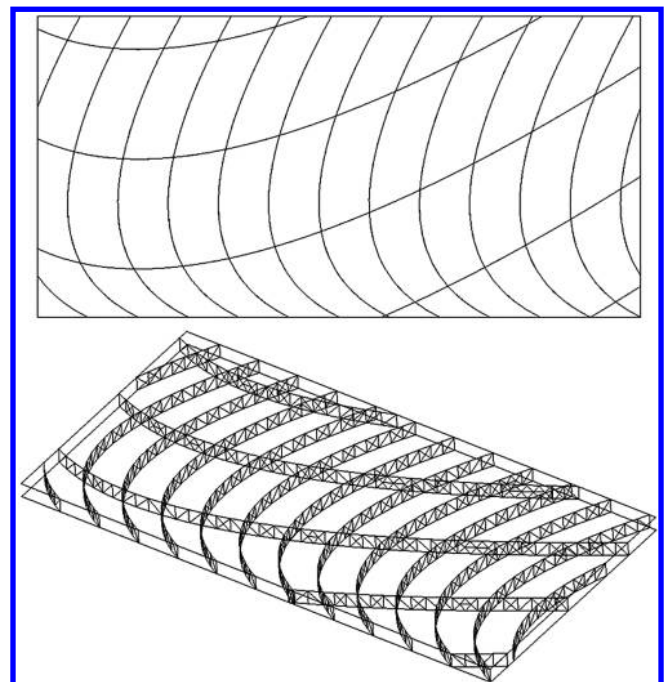


Fig. 15 Internal structure of rectangular wing optimized using curvilinear SpaRibs and one-step optimization: case II.

Table 12 DV results for the rectangular wing optimized using curvilinear SpaRibs and two-step optimization framework

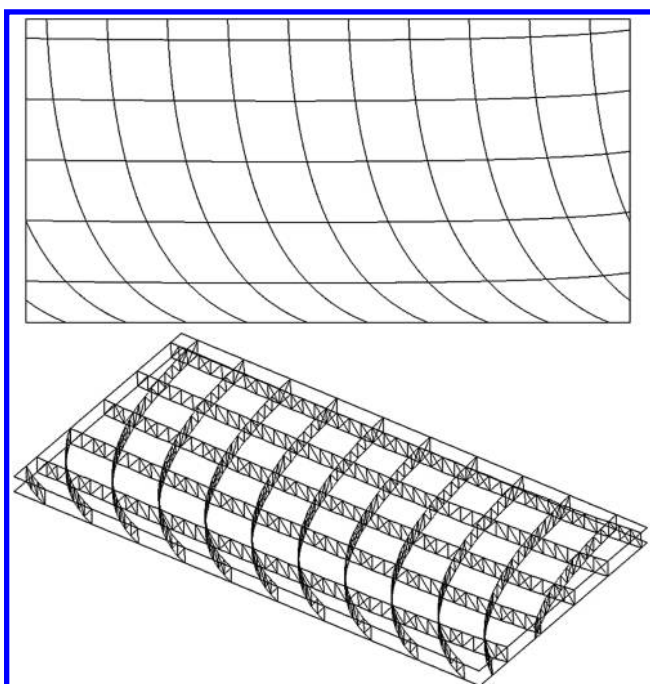
Design variable	Optimized	Baseline
Upper-skin thickness, in.	0.033	0.06
Lower-skin thickness, in.	0.015	0.06
Spar thickness, in.	0.037	0.04
Rib thickness, in.	0.036	0.04
Spar start-point x coordinate, in.	8.000	2.5
Spar control-point x coordinate, in.	3.000	2.5
Spar control-point y coordinate, in.	5.000	7.5
Spar endpoint x coordinate, in.	1.006	2.5
Spar distance, in.	3.000	5.0
Rib start-point y coordinate, in.	2.053	1.85
Rib control-point x coordinate, in.	20.000	15.0
Rib control-point y coordinate, in.	2.000	1.85
Rib endpoint y coordinate, in.	2.470	1.85
Rib distance, in.	3.000	11.3
Responses		
W , lb	3.22	5.91
BF_0	0.752	0.587
KSC_σ	N/A	N/A

deformation and the mode shapes and frequencies of these structures are different, leading to different dynamic and aeroelastic behaviors.

The optimized structures designed using one-step-framework optimization are certainly not optimal solutions from the weight point of view. Indeed, the bigrid optimal designs found are 22 to 38% lighter than the curvilinear SpaRibs optima. In an attempt to design a better structure, the two-step optimization framework was applied, and Table 12 and Fig. 16 show, respectively, the DV vector and the internal topology of the optimum design. This structure is different from the two mentioned above. Moreover, the weight of the wing is 3.22 lb and is the minimum found so far for this structure (Table 13).

Table 13 summarizes the curvilinear SpaRibs optima found for the rectangular wing box. The best configuration is the one obtained with the two-step optimization framework, and although the CPU time is slightly higher for this analysis than for the one-step optimization analysis cases, we believe this is a fair tradeoff to reach a better design.

The von Mises stress distribution and the buckling fundamental eigenvalue are plotted in Fig. 17 for the baseline configuration and

**Fig. 16 Internal structure of rectangular wing optimized using curvilinear SpaRibs and two-step optimization.****Table 13 W , BF_0 , KSC_σ , n_{iter} , and T_{CPU} for the baseline and the three optimum wing configurations found**

	Baseline	One-step case I	One-step case II	Two-step case
W lb	5.91	4.62	4.19	3.22
BF_0^a	0.591	0.699	0.752	0.752
KSC_σ	N/A	0.284	0.233	N/A
n_{iter}	N/A	1000	1465	903
T_{CPU}	N/A	8 h	8 h	9 h

^aA safety factor of 1.33 was used for the formulation of the buckling-factor constraint.

the three optimal designs to note the differences in the load-carrying and static instability capabilities. In particular, the buckling fundamental eigenvalue plot shows how the local instability of the wing skin panels is located in different regions of the wing box for each configuration. The instability pocket size is reduced in the optimized configurations, when compared with the baseline, and its position migrates from the trailing edge toward the center of the wing.

B. Generic Supersonic Fighter Wing

The rectangular wing-box case was a good start to set in place and test the optimization framework. However, in reality, more complex cases, in terms of geometry generation and FE modeling, are encountered daily by the designers. A more complex application case was then required. ZONA Technology, Inc., provided us with the geometry and internal configuration of a generic supersonic fighter type of wing, and we were able to apply our framework to this case. The results are presented in the following.

The wing planform and the internal topology with 10 straight spars and 10 straight ribs are visualized in Figs. 18 and 19. For the lack of CFD-generated loads, we applied a uniform pressure distribution corresponding to a wing load of 14.85 psi and load factor of 9. The material used is aluminum alloy 2124 T851, for which the mechanical properties are listed in Table 5).

To compare the optimization results with the baseline wing, we first generated an optimum baseline design, optimizing the thicknesses of the skin panels, the spars, and the ribs of the original structure without changing its topology. One-step and two-step frameworks were applied with the PSO optimization method with a population size of five particles. Figure 20 shows the two optima found.

The two designs are very similar to each other, with both including 17 spars and four ribs. This is expected, since the optimization starting point and the DV boundaries are the same in both cases. This shows the consistency of the two frameworks. The structure weight is slightly different and, more important, it is reduced if compared with the weight of the baseline wing (Table 14). Figure 21 shows the von Mises stress distribution and the buckling mode shape for the baseline wing and the two optimized configurations. The instability pocket has approximately the same size and position for the three designs presented. The wing stiffness improvement is due solely to the buckling mode shape changes driven by the curvilinear SpaRibs

The last result we want to present is a one-step optimization analysis carried out using PSO with a population size of 20 particles. The population size is a critical parameter for PSO [36,38,39], and we wanted to investigate the impact of changing the number of particles in the swarm. A large swarm is usually preferred to a small swarm; however, using too many particles can quickly degrade the performance in terms of the T_{CPU} . In other words, a small loss in the accuracy of the optimum design may be preferred to a significantly more time-consuming optimization with a large swarm. Table 15 shows the result for this case compared with the one-step optimization with PSO and five particles in the swarm.

Clearly, in this case there is no advantage in using a larger swarm of particles, since we found an optimum design slightly better than the previous (and yet, not a better one than the two-step optimization optimum), but using more than 16 times the computational resources.

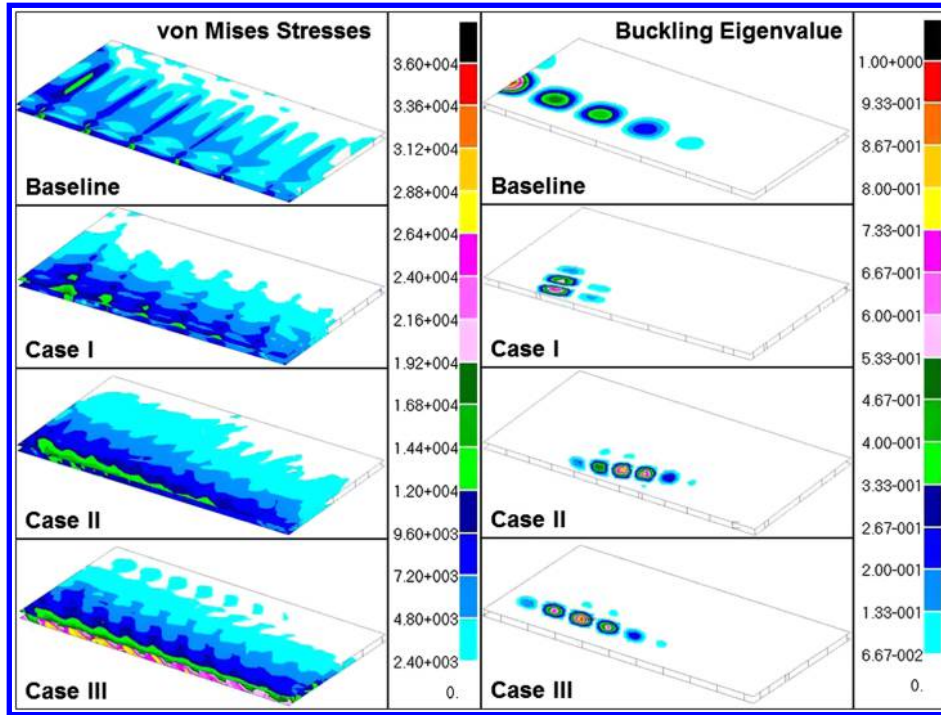


Fig. 17 Von Mises stress distribution and buckling fundamental eigenvalue for the rectangular wing-box optimization with curvilinear SpaRibs. The baseline structure is compared with the optimized configurations.

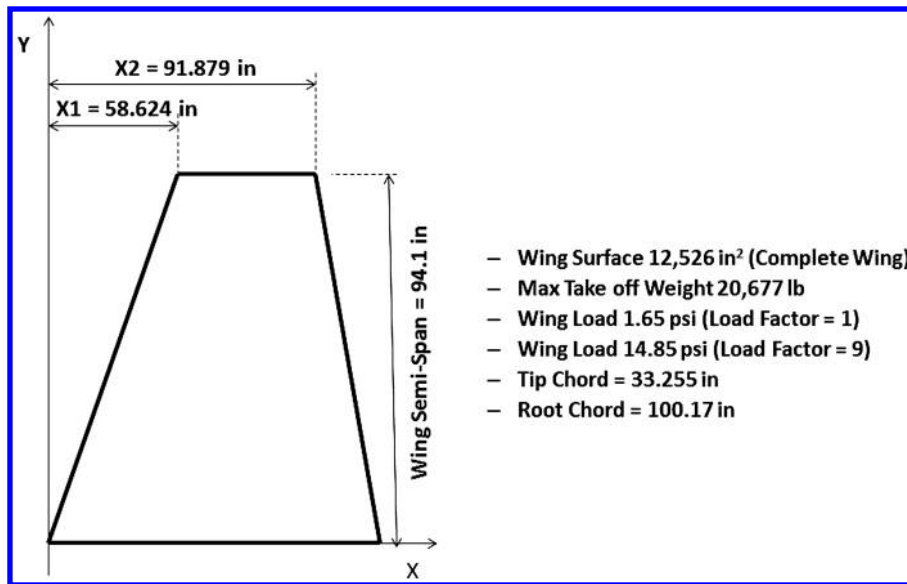


Fig. 18 Generic supersonic fighter wing planform provided by ZONA Technology, Inc.

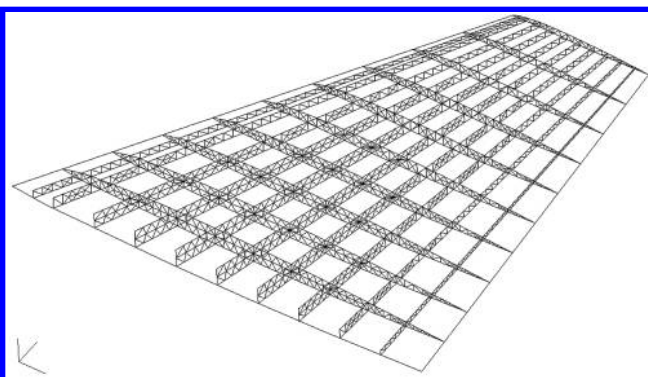


Fig. 19 Generic supersonic fighter wing geometry and internal topology provided by ZONA Technology, Inc.

VI. Conclusions

In this paper a new optimization schema was presented that includes topology and sizing optimization, carried out together or separately. The method has proven to be effective, efficient, and consistent for finding optimal designs of winglike structures characterized by the use of SpaRibs. In both the example cases considered, we were able to find lighter airframe designs using curvilinear SpaRibs, as compared with the classical designs with straight spars and ribs.

This work has to be integrated with a much larger frame in which the design of a structure is carried out in a collaborative and in a synergetic way by taking into account all disciplines involved with their respective objective functions and constraint. This paper is the first step toward this design philosophy. The future actions to be taken are essentially directed toward two objectives. The first objective is to keep improving the geometry generation and the

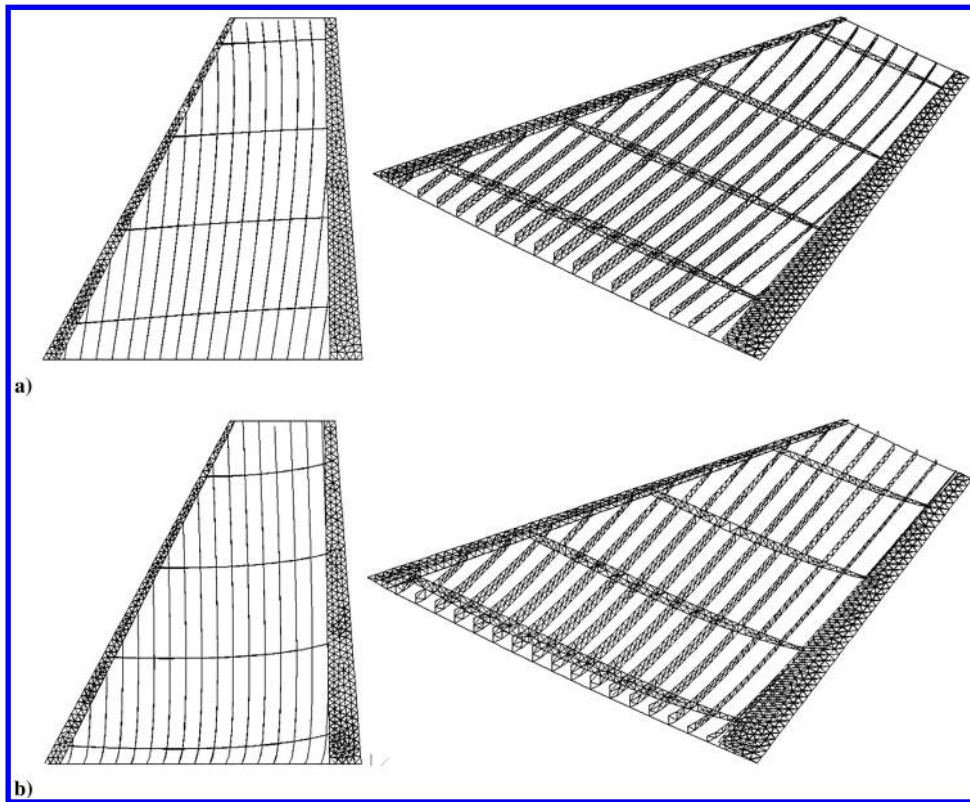


Fig. 20 Generic supersonic fighter wing geometry optimal configurations: a) one-step optimum and b) two-step optimum.

Table 14 W , BF_0 , KSC_σ , n_{iter} , and T_{CPU} for the three optima wing configurations found compared with the baseline structure

	Baseline	One-step case	Two-step case
W lb	399.4	346.0	323.9
BF_0	0.752	0.752	0.752
KSC_σ	N/A	0.969	1.0
n_{iter}	N/A	435	632
T_{CPU}	N/A	5 h	8 h

remeshing tool to reach the ability to automatically regenerate very complex structures and FE models. This has to be done by keeping in mind the requirements of the optimizer, which ultimately drives the parameterization of the structure. An example is shown in Fig. 22, where the parameterization of the SpaRibs has been changed to a higher-order B-spline curve. The second objective, probably the more challenging, is to integrate new disciplines such as CFD analysis, thermal analysis, flutter and dynamics analysis, etc., in the current framework, which means being able to efficiently integrate

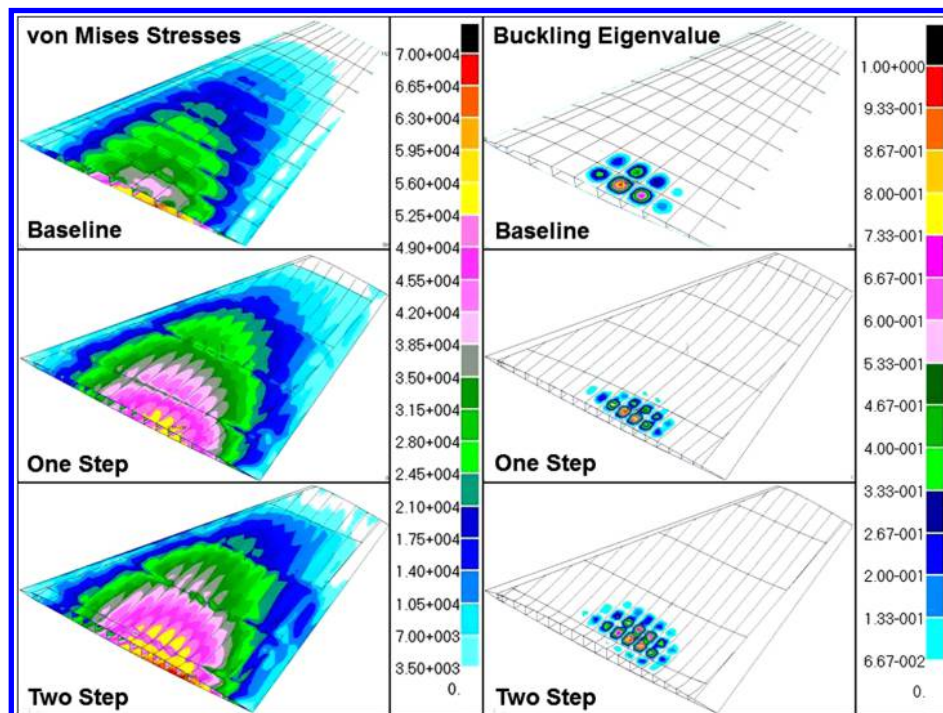


Fig. 21 Generic supersonic fighter wing stress distribution and buckling mode shape. The baseline structure is compared with the two optimized configurations.

Table 15 W , BF_0 , KSC_σ , n_{iter} , and T_{CPU} for the one-step optimization of the generic supersonic fighter wing using PSO and different population sizes

	One-step case (5 particles)	One-step case (20 particles)
W lb	346.0	335.7
BF_0	0.752	0.752
KSC_σ	0.969	0.719
n_{iter}	435	6005
T_{CPU}	5 h	81 h

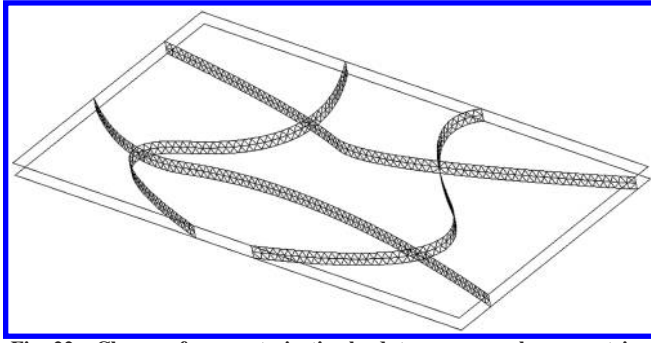


Fig. 22 Change of parameterization leads to more complex geometries.

different software packages that use different formats of inputs and outputs.

Acknowledgments

The authors would like to thank Marcia S. Domack, Karen Taminger, and the electron beam free-form fabrication (EBF³) team at NASA Langley Research Center for technical discussions and for sponsoring this research through the National Institute of Aerospace, Hampton, Virginia. The authors also thanks John E. Barnes, Ryan J. Wittman, and Augustine Garcia at Lockheed Martin Aeronautics Company for suggesting the dimensions of the rectangular wing and load cases. A special thanks goes to ZONA Technology, Inc., Scottsdale, Arizona, for the help received in understanding how to include aeroelastic analysis in our future framework and for ZAERO technical support.

References

- [1] Renton, W. J., Olcott, D., Roeseler, W., Batzer, R., Baron, W., and Velicki, A., "Future of Flight Vehicle Structures (2002–2023)," *Journal of Aircraft*, Vol. 41, No. 5, 2004, pp. 986–998. doi:10.2514/1.4039
- [2] Chan, K., Harter, J., Grandt, A. F., and Honeycutt, K., "Enhanced Crack Growth Methodology and Analyses for Unitized Structures," *Ninth Joint FAA/DoD/NASA Conference on Aging Aircraft*, Atlanta, 6–9 March 2006.
- [3] Pettit, R. G., Wang, J. J., and Toth, C., "Validated Feasibility Study of Integrally Stiffened Metallic Fuselage Panels for Reducing Manufacturing Costs," NASA CR-2000-209342, 2000.
- [4] Buswell, R. A., Soar, R. C., Gibb, A. G. F., and Thorpe, A., "Freeform Construction: Mega-Scale Rapid Manufacturing for Construction," *Automation in Construction*, Vol. 16, 2007, pp. 224–231. doi:10.1016/j.autcon.2006.05.002
- [5] Cooper, K., Crocket, R., and Roberts, F., "Free Form Fabrication in Space," *42nd AIAA Aerospace Science Meeting and Exhibition*, AIAA Paper 2004-1307, Reno, NV, 5–8 Jan. 2004.
- [6] Nicholas, E. D., "Developments in the Friction-Stir Welding of Metals," *ICAA-6: 6th International Conference on Aluminium Alloys*, 1998.
- [7] Taminger, K. M. B., and Hafley, R. A., "Electron Beam Freeform Fabrication: A Rapid Metal Deposition Process," *Proceedings of 3rd Annual Automotive Composites Conference*, Society of Plastic Engineers, Troy, MI, 9–10 Sept. 2003.
- [8] Taminger, K. M. B., and Hafley, R. A., "Characterization of 2219 Aluminum Produced by Electron Beam Freeform Fabrication," *Proceedings of 13th SFF Symposium*, 2002, pp. 482–489.
- [9] Taminger, K. M. B., Hafley, R. A., and Dicus, D. L., "Solid Freeform Fabrication: An Enabling Technology for Future Space Missions,"

Keynote Lecture for 2002 International Conference on Metal Powder Deposition for Rapid Manufacturing, Metal Powder Industries Federation, San Antonio, TX, April 8–10, 2002, pp. 51–56.

- [10] Bendsoe, M., and Kikuchi, N., "Generating Optimal Topologies in Optimal Design Using a Homogenization Method," *Computer Methods in Applied Mechanics and Engineering*, Vol. 71, 1988, pp. 197–224. doi:10.1016/0045-7825(88)90086-2
- [11] Niu, M. C. Y., *Airframe Stress Analysis and Sizing*, Hong Kong Conmil Press, Hong Kong, 1999.
- [12] Gürdal, Z., and Gendron, G., "Optimal Design of Geodesically Stiffened Composite Cylindrical Shells," *Composites Engineering*, Vol. 3, No. 12, 1993, pp. 1131–1147. doi:10.1016/0961-9526(93)90070-Z
- [13] Gürdal, Z., and Grall, B., "Buckling Analysis of Geodesically Stiffened Composite Panels with Discrete Stiffeners," *Journal of Aircraft*, Vol. 31, No. 5, Sept.–Oct. 1994, pp. 1197–1204. doi:10.2514/3.46630
- [14] Gendron, G., and Gürdal, Z., "Optimal Design of Geodesically Stiffened Composite Cylindrical Shells," *33rd AIAA/ASME/ASCE/AHS/ASC Structures, Structural Dynamics and Materials Conference*, AIAA, Washington, D.C., Apr. 1992, pp. 2431–2441.
- [15] Grall, B., and Gürdal, Z., "Structural Analysis And Design of Geodesically Stiffened Panels with Variable Stiffener Distribution," NASA CR-190608, 1992.
- [16] "Isogrid Design Handbook," Rev. A NASA CR-124075, Feb. 1973.
- [17] Wegner, P., Ganley, J., Huybrechts, S., and Meink, T., "Advanced Grid Stiffened Composite Payload Shroud for the OSP Launch Vehicle," *IEEE Aerospace Conference Proceedings*, Vol. 4, IEEE Press, Piscataway, NJ, 2000, pp. 359–365.
- [18] Huybrechts, S., and Tsai, S. W., "Analysis and Behavior of Grid Structures," *Composites Science and Technology*, Vol. 56, 1996, pp. 1001–1015. doi:10.1016/0266-3538(96)00063-2
- [19] Jaunky, N., Knight, N. F. J., and Ambur, D., "Optimal Design of Grid-Stiffened Composite Panels Using Global and Local Buckling Analysis," *37th AIAA/ASME/ASCE/AHS/ASC Structures, Structural Dynamics and Materials Conference and Exhibit*, Apr. 15–17 1996, pp. 2315–2325; also AIAA Paper 96-1581.
- [20] Paul, D., Kelly, L., and Venkayya, V., "Evolution of U. S. Military Aircraft Structures Technology," *Journal of Aircraft*, Vol. 39, No. 1, Jan.–Feb. 2002, pp. 18–29. doi:10.2514/2.2920
- [21] Blom, A. W., Reassian, M., Stickler, P., and Gürdal, Z., "Modal Testing of a Composite Cylinder with Circumferentially Varying Stiffness," *50th AIAA/ASME/ASCE/AHS/ASC Structures, Structural Dynamics, and Materials Conference*, AIAA Paper 2009-2558, Palm Springs, CA, 4–7 May 2009.
- [22] Chen, P. C., Jha, R., Sarhaddi, D., Liu, D. D., Griffin, K., and Yurkovich, R., "A Variable Stiffness Spar (VSS) Approach for Aircraft Maneuver Enhancement Using ASTROS," *AIAA/ASME/ASCE/AHS/ASC Structures, Structural Dynamics, and Materials Conference and Exhibit*, Vol. 3, AIAA, Reston, VA, 12–15 Apr. 1999, pp. 2233–2241.
- [23] Onoda, J., Endo, T., Tamaoki, H., and Watanabe, N., "Vibration Suppression by Variable-Stiffness Members," *31st AIAA/ASME/ASCE/AHS/ASC Structures, Structural Dynamics and Materials Conference*, AIAA, Washington, D.C., 2–4 Apr. 1990, pp. 2359–2366.
- [24] Kobayashi, M. H., Pedro, H. T. C., Reich, G. W., and Kolonay, R. M., "On a Cellular Division Model for Topology Optimization," *50th AIAA/ASME/ASCE/AHS/ASC Structures, Structural Dynamics, and Materials Conference*, AIAA Paper 2009-2102, Palm Springs, CA, 4–7 May 2009.
- [25] Kobayashi, M. H., LeBon, A., Pedro, H. T. C., Kolonay, R. M., and Reich, G. W., "On a Cellular Division Model for Multi-Disciplinary Optimization," *51th AIAA/ASME/ASCE/AHS/ASC Structures, Structural Dynamics, and Materials Conference*, AIAA Paper 2010-2989, Orlando, FL, 12–15 April 2010.
- [26] Kolonay, R. M., and Kobayashi, M. H., "Topology, Shape, and Sizing Optimization of Aircraft Lifting Surfaces Using a Cellular Division Method," *13th AIAA/ISSMO Multidisciplinary Analysis Optimization Conference*, AIAA Paper 2010-9079, Fort Worth, TX, 13–15 Sept. 2010.
- [27] Love, A. E. H., *A Treatise on the Mathematical Theory of Elasticity*, Dover, New York, 1944.
- [28] MATLAB, Software Package, Version 7.6.0.324 (R2008a), MathWorks, Inc., Natick, MA, 2008.
- [29] VisualDOC, Software Package, Version 6.1, Vanderplaats Research and Development, Colorado Springs, CO, 2008.
- [30] MD.PATRAN, Software Package, Version 2008 r1, MSC Software, Santa Ana, CA, 2008.

- [31] MD.NASTRAN, Software Package, Version R2.1, MSC Software, Santa Ana, CA, 2008.
- [32] Gurav, S. P., and Kapania, R. K., "Development of Framework for the Design Optimization of Unitized Structures," 50th AIAA/ASME/ASCE/AHS/ASC Structures, Structural Dynamics, and Materials Conference, AIAA Paper 2009-2186, Palm Springs, CA, 4–7 May 2009.
- [33] Schramm, U., Zhou, M., Tang, P. S., and Harte, C., "Topology Layout for Structural Designs and Buckling," 10th AIAA/ISSMO Multidisciplinary Analysis and Optimization Conference, AIAA Paper 2004-4636, Albany, NY, Aug. 30–Sept. 1 2004.
- [34] Mulani, S. B., Li, J., Joshi, P., and Kapania, R. K., "Optimization of Stiffened Electron Beam Freeform Fabrication (EBF3) Panels Using Response Surface Approaches," 48th AIAA/ASME/ASCE/AHS/ASC Structures, Structural Dynamics and Materials Conference, AIAA Paper 2007-1901, Honolulu, 23–26 April 2007.
- [35] Mulani, S. B., Joshi, P., Li, J., Kapania, R. K., and Shin, Y., "Optimal Design of Unitized Structures with Curvilinear Stiffeners Using Response Surface Approaches," *Journal of Aircraft*, Vol. 47, No. 6, Nov.–Dec. 2010, pp. 1898–1906.
doi:10.2514/1.47411
- [36] Mulani, S. B., Locatelli, D., and Kapania, R. K., "Algorithm Development for Optimization of Arbitrary Geometry Panels Using Curvilinear Stiffeners," 51st AIAA/ASME/ASCE/AHS/ASC Structures, Structural Dynamics and Materials Conference, AIAA Paper 2010-2674, 10–15 April 2010.
- [37] Kreisselmeier, G., and Steinhauser, R., "Systematic Control Design by Optimizing a Vector Performance Index," *Proceedings of the IFAC Symposium on Computer-Aided Design of Control Systems*, Zurich, 1979, pp. 113–117.
- [38] Venter, G., and Sobieszczanski-Sobieski, J., "Multidisciplinary Optimization of a Transport Aircraft Wing Using Particle Swarm Optimization," 9th AIAA/ISSMO Symposium on Multidisciplinary Analysis and Optimization, AIAA Paper 2002-644, Atlanta, 4–6 Sept. 2002.
- [39] Venter, G., and Sobieszczanski-Sobieski, J., "Particle Swarm Optimization," *AIAA Journal*, Vol. 41, No. 8, 2003, pp. 1583–1589.
doi:10.2514/2.2111

This article has been cited by:

1. Ramana V. Grandhi, Hao Li, Marcelo Kobayashi, Raymond M. Kolonay. Vehicle Configuration Design Using Cellular-Division and Level-Set Based Topology Optimization 29-40. [[Crossref](#)]
2. Gunther Moors, Christos Kassapoglou, Sergio Frascino Müller de Almeida, Clovis Augusto Eça Ferreira. 2018. Weight trades in the design of a composite wing box: effect of various design choices. *CEAS Aeronautical Journal* 4. . [[Crossref](#)]
3. Mohammad Raheel, Vassili Toropov. Topology Optimization of an Aircraft Wing with an Outboard X-Stabilizer . [[Citation](#)] [[PDF](#)] [[PDF Plus](#)]
4. Max M. Opgenoord, Karen E. Willcox. Aeroelastic Tailoring using Additively Manufactured Lattice Structures . [[Citation](#)] [[PDF](#)] [[PDF Plus](#)]
5. Rikin Gupta, Nathan J. Love, Rakesh K. Kapania, David Schmidt. Development of Longitudinal Flight Dynamics Analysis Framework with Controllability and Observability Metrics . [[Citation](#)] [[PDF](#)] [[PDF Plus](#)]
6. Wei Zhao, Rakesh K. Kapania. Multiobjective Optimization of Composite Flying-wings with SpaRibs and Multiple Control Surfaces . [[Citation](#)] [[PDF](#)] [[PDF Plus](#)]
7. Scott Townsend, Bret Stanford, Sandilya Kambampati, Hyunsun A. Kim. Aeroelastic Optimization of Wing Skin using a Level Set Method . [[Citation](#)] [[PDF](#)] [[PDF Plus](#)]
8. Bret K. Stanford. 2018. Aeroelastic Wingbox Stiffener Topology Optimization. *Journal of Aircraft* 55:3, 1244-1251. [[Abstract](#)] [[Full Text](#)] [[PDF](#)] [[PDF Plus](#)]
9. Arthur Dubois, Charbel Farhat, Abdullah H. Abukhwejah, Hesham Mohamed Shageer. 2018. Parameterization Framework for the MDAO of Wing Structural Layouts. *AIAA Journal* 56:4, 1627-1638. [[Abstract](#)] [[Full Text](#)] [[PDF](#)] [[PDF Plus](#)]
10. Zhijun Liu, Shingo Cho, Akihiro Takezawa, Xiaopeng Zhang, Mitsuru Kitamura. 2018. Two-stage layout-size optimization method for prow stiffeners. *International Journal of Naval Architecture and Ocean Engineering* . [[Crossref](#)]
11. Elliot K. Bontoft, Vassili Toropov. Topology Optimisation of Multi-Element Wingtip Devices . [[Citation](#)] [[PDF](#)] [[PDF Plus](#)]
12. Bret Stanford, Christine V. Jutte, Christian Coker. Sizing and Layout Design of an Aeroelastic Wingbox through Nested Optimization . [[Citation](#)] [[PDF](#)] [[PDF Plus](#)]
13. Wei Zhao, Rakesh K. Kapania. BLP Optimization of Composite Flying-wings with SpaRibs and Multiple Control Surfaces . [[Citation](#)] [[PDF](#)] [[PDF Plus](#)]
14. Sandilya Kambampati, Scott Townsend, Hyunsun A. Kim. Aeroelastic Level Set Topology Optimization for a 3D Wing . [[Citation](#)] [[PDF](#)] [[PDF Plus](#)]
15. David J. Munk, Dries Verstraete, Gareth A. Vio. 2017. Effect of fluid-thermal-structural interactions on the topology optimization of a hypersonic transport aircraft wing. *Journal of Fluids and Structures* 75, 45-76. [[Crossref](#)]
16. Weizhu Yang, Zhufeng Yue, Lei Li, Fan Yang, Peiyan Wang. 2017. Optimization design of unitized panels with stiffeners in different formats using the evolutionary strategy with covariance matrix adaptation. *Proceedings of the Institution of Mechanical Engineers, Part G: Journal of Aerospace Engineering* 231:9, 1563-1573. [[Crossref](#)]
17. Bret Stanford. Aeroelastic Wingbox Stringer Topology Optimization . [[Citation](#)] [[PDF](#)] [[PDF Plus](#)]
18. Mohamed Jrad, Shuvodeep De, Rakesh K. Kapania. Global-local Aeroelastic Optimization of Internal Structure of Transport Aircraft wing . [[Citation](#)] [[PDF](#)] [[PDF Plus](#)]
19. X.C. Qin, C.Y. Dong, F. Wang, X.Y. Qu. 2017. Static and dynamic analyses of isogeometric curvilinearly stiffened plates. *Applied Mathematical Modelling* 45, 336-364. [[Crossref](#)]
20. Wei Zhao, Rakesh K. Kapania. 2017. Vibration Analysis of Curvilinearly Stiffened Composite Panel Subjected to In-Plane Loads. *AIAA Journal* 55:3, 981-997. [[Abstract](#)] [[Full Text](#)] [[PDF](#)] [[PDF Plus](#)]
21. John T. Hwang, Joaquim R.R.A. Martins. 2016. An unstructured quadrilateral mesh generation algorithm for aircraft structures. *Aerospace Science and Technology* 59, 172-182. [[Crossref](#)]
22. Qiang Liu, Mohamed Jrad, Sameer B. Mulani, Rakesh K. Kapania. 2016. Global/Local Optimization of Aircraft Wing Using Parallel Processing. *AIAA Journal* 54:11, 3338-3348. [[Abstract](#)] [[Full Text](#)] [[PDF](#)] [[PDF Plus](#)]
23. Peng Hao, Bo Wang, Kuo Tian, Gang Li, Xi Zhang. 2016. Optimization of Curvilinearly Stiffened Panels with Single Cutout Concerning the Collapse Load. *International Journal of Structural Stability and Dynamics* 16:07, 1550036. [[Crossref](#)]

24. Teemu J. Ikonen, Andras Sobester. Ground Structure Approaches for the Evolutionary Optimization of Aircraft Wing Structures . [[Citation](#)] [[PDF](#)] [[PDF Plus](#)]
25. P. Hao, B. Wang, K. Tian, G. Li, K. Du, F. Niu. 2016. Efficient Optimization of Cylindrical Stiffened Shells with Reinforced Cutouts by Curvilinear Stiffeners. *AIAA Journal* **54**:4, 1350-1363. [[Abstract](#)] [[Full Text](#)] [[PDF](#)] [[PDF Plus](#)]
26. Guillaume Francois, Jonathan E. Cooper, Paul Weaver. Impact of the Wing Sweep Angle and Rib Orientation on Wing Structural Response for Un-Tapered Wings . [[Citation](#)] [[PDF](#)] [[PDF Plus](#)]
27. Arthur Dubois, Charbel Farhat, Abdullah H. Abukhwejah. Parameterization Framework for Aeroelastic Design Optimization of Bio-Inspired Wing Structural Layout . [[Citation](#)] [[PDF](#)] [[PDF Plus](#)]
28. Wei Zhao, Rakesh K. Kapania. Vibrational Analysis of Unitized Curvilinearly Stiffened Composite Panels Subjected to In-plane Loads . [[Citation](#)] [[PDF](#)] [[PDF Plus](#)]
29. Wei Zhao, Rakesh K. Kapania. 2016. Buckling analysis of unitized curvilinearly stiffened composite panels. *Composite Structures* **135**, 365-382. [[Crossref](#)]
30. Shutian Liu, Quhao Li, Wenjiong Chen, Rui Hu, Liyong Tong. 2015. H-DGTP—a Heaviside-function based directional growth topology parameterization for design optimization of stiffener layout and height of thin-walled structures. *Structural and Multidisciplinary Optimization* **52**:5, 903-913. [[Crossref](#)]
31. Bret K. Stanford, Peter D. Dunning. 2015. Optimal Topology of Aircraft Rib and Spar Structures Under Aeroelastic Loads. *Journal of Aircraft* **52**:4, 1298-1311. [[Abstract](#)] [[Full Text](#)] [[PDF](#)] [[PDF Plus](#)]
32. Robert E. Bartels, Pawel Chwalowski, Christie Funk, Jennifer Heeg, Jiyoung Hur, Mark D. Sanetrik, Robert C. Scott, Walter A. Silva, Bret Stanford, Carol D. Wieseman. Ongoing Fixed Wing Research within the NASA Langley Aeroelasticity Branch . [[Citation](#)] [[PDF](#)] [[PDF Plus](#)]
33. Davide Locatelli, Sameer B. Mulani, Rakesh K. Kapania. 2014. Parameterization of Curvilinear Spars and Ribs for Optimum Wing Structural Design. *Journal of Aircraft* **51**:2, 532-546. [[Abstract](#)] [[Full Text](#)] [[PDF](#)] [[PDF Plus](#)]



Nonstationary Random Vibration Analysis of Wing with Geometric Nonlinearity Under Correlated Excitation

Yanbin Li*

Southeast University, Jiangsu 211189, People's Republic of China

Sameer B. Mulani[†]

The University of Alabama, Tuscaloosa, Alabama 35487

Rakesh K. Kapania[‡]

Virginia Polytechnic Institute and State University, Blacksburg, Virginia 24060

and

Qingguo Fei[§] and Shaoqing Wu[¶]

Southeast University, Jiangsu 211189, People's Republic of China

DOI: 10.2514/1.C034721

An algorithm that integrates Karhunen-Loeve expansion (KLE), nonlinear finite element method (NFEM), and a sampling technique to quantify the uncertainty is proposed to carry out random vibration analysis of a structure with geometric nonlinearity under correlated nonstationary random excitations. In KLE, the eigenvalues and eigenfunctions of the autocovariance are obtained by using orthogonal basis functions, and the KLE for correlated random excitations relies on expansions in terms of correlated sets of random variables. The autocovariance functions of excitation are discretized into a series of correlated excitations, and then the structural response is carried out by using NFEM and sampling techniques. The proposed algorithm is applied to both rigid and flexible aircraft wings. Two different types of the boundary condition are studied for the flexible wing: fixed and large mass method (LMM). Results show that the geometric nonlinearity has a stiffening effect on the behavior of the aircraft wing, resulting in an oscillatory response with a lower amplitude, and changes the distribution of the random responses. The response due to LMM boundary condition that is closer to the actual conditions is smaller than the response obtained using fixed boundary condition.

Nomenclature

A	=	load application area
B	=	turbulence length scale
C	=	damping matrix
$C_{F_i F_i}$	=	autocovariance of the excitation
$C_{F_i F_j}$	=	cross-covariance of the excitation
c, α, β	=	parameters of nonstationary gust
$d_{jk}^{(i)}$	=	participation factor of $h_j^{(i)}$ basis function for $\phi_k^{(i)}$ eigenvector
$F(t, \omega)$	=	distributed forcing excitation
$f(t, \omega)$	=	discrete forcing excitation
$G(t)$	=	zero stationary Gaussian random process
$H(x)$	=	nonlinear stiffness matrix
$h_j^{(i)}$	=	Karhunen-Loeve basis function
K	=	stiffness matrix
$k_{km}^{(ij)}$	=	correlation of the random variables
l_1, l_2	=	spatial correlation parameter
M	=	mass matrix
N	=	shape function of system

NE	=	element number
P	=	correlation matrix
$R_{X_i X_i}$	=	autocovariance of the response
S	=	wing area
$S_{F_i F_i}$	=	power spectral density function of the excitation
T	=	transfer matrix that forms element coordinates to global coordinates
U	=	velocity of aircraft
V	=	velocity of wing
W	=	velocity of gust
x	=	displacement
y_i	=	the bound of a subdomain of aircraft
γ	=	eigenvalues of the correlation matrix P
γ_1, γ_2	=	decay rates in the streamwise and spanwise directions
ζ	=	a vector of independent standard Gaussian random variables
$\lambda_k^{(i)}$	=	eigenvalues of the autocovariance function
$\mu_F^{(i)}$	=	mean values of the random processes $f_i(t, \omega)$
ζ_1, ζ_2	=	separation distances in the streamwise and spanwise directions
$\xi_k^{(i)}$	=	sets of correlated random variables
ρ	=	density of air
$\sigma_{X_i X_i}$	=	standard deviation of the displacement
τ_i, τ_{ij}	=	autocorrelation length and cross-correlation length
ϕ	=	eigenvectors of the correlation matrix P
$\phi_k^{(i)}$	=	eigenvectors of the autocovariance function
ω	=	sample space in the frequency

Received 23 August 2017; revision received 28 February 2018; accepted for publication 15 April 2018; published online 6 July 2018. Copyright © 2018 by Y. Li, S. B. Mulani, R. K. Kapania, Q. Fei, and S. Wu. Published by the American Institute of Aeronautics and Astronautics, Inc., with permission. All requests for copying and permission to reprint should be submitted to CCC at www.copyright.com; employ the ISSN 0021-8669 (print) or 1533-3868 (online) to initiate your request. See also AIAA Rights and Permissions www.aiaa.org/randp.

*Assistant Professor, School of Mechanical Engineering, Institute of Aerospace Machinery and Dynamics, Nanjing; lyb@seu.edu.cn.

[†]Assistant Professor, Department of Aerospace Engineering and Mechanics; sbmulani@eng.ua.edu. Senior Member AIAA.

[‡]Mitchell Professor, Kevin T. Crofton Department of Aerospace and Ocean Engineering; rkapania@vt.edu. Lifetime Associate Fellow AIAA.

[§]Professor, School of Mechanical Engineering, Institute of Aerospace Machinery and Dynamics, Nanjing; qgfei@seu.edu.cn.

[¶]Associate Professor, Department of Engineering Mechanics, Nanjing; cesqw@seu.edu.cn.

I. Introduction

MANY engineering structures are subjected to random dynamic excitations that might be uncorrelated or correlated in time and/or in space. Random excitations, which lack a deterministic definition in time and/or space, often occurs in many real-life vibration problems, for example, gust loads on aircraft wings, excitations caused by turbulent boundary layers on panels, and nonstationary wind and seismic loads on civil structures. The correlated random processes are often simplified to be stationary,

Gaussian, and uncorrelated processes for the convenience of a random vibration analysis. However, many engineering structures encounter nonstationary and correlated random excitations.

Most of the previous studies on random vibration were confined to linear systems that are restricted to small deformations where geometric nonlinearities were not considered for larger complex systems [1]. It is necessary to consider geometric nonlinear effects to get the realistic behavior of the structures where large deformation occurs. For flexible structures such as aircraft, satellites, bridges, and tall/slender structures, the large out-of-plane deformation results in the presence of in-plane stretching. Hence, nonlinearities may significantly change the dynamic structural response behavior. Moreover, nonlinear random vibration analysis has been drawing increasing attention in recent years to design many civil, mechanical, and aerospace structures [2]. However, nonlinear random vibration analysis under nonstationary correlated random processes has not been studied in great depth. The nonlinear random vibration analysis is conducted by analytical and numerical methods [3]. Analytical methods have been used to carry out the nonlinear random vibration analysis under nonstationary random excitations [4–6] for simple systems. For large complex systems, the development of nonlinear random vibration analysis under nonstationary correlated excitations is inhibited by both the extensive computational cost and the inherent mathematical intricacies. With the relentless progress in high-performance computing, computational methods are being increasingly used to perform nonlinear random vibration analyses [7].

Random processes can be described using covariance functions, and the power spectral density (PSD) functions in time and frequency domain, respectively. For stationary processes, PSD functions are usually adopted to define the random processes [8–10]. For nonstationary processes, marginal probability density functions (PDF) of the excitation may only have positive real domains that might be bounded. Therefore, the covariance functions are used to represent the random processes in the time domain. For most of the random vibration analysis, it is necessary to decompose the continuous random processes of excitation when autocovariance functions are used to define the random excitations [11]. Efforts have been made to decompose the autocovariance by using Karhunen-Loeve expansion (KLE) [12], and polynomial chaos expansion [13]. The KLE is a useful and efficient tool for discretizing second-order random processes with known covariance function. However, the efficiency and accuracy of KLE for discretizing random processes highly depends on the accurate eigenvalues and eigenfunctions of the autocovariance functions [14]. An algorithm using decomposition using orthogonal polynomials to represent the autocovariance function has been proposed [1,15,16]. However, it often yields negative eigenvalues based upon the selection of the type of basis functions. Therefore, it is critical to select a suitable set of basis functions in KLE. In the authors' previous work [17,18], two different basis functions for KLE have been chosen: the global trigonometric basis functions and the piecewise linear basis functions. The piecewise basis functions are efficient and do not yield negative and/or infinite eigenvalues for the autocovariance function.

If random processes are uncorrelated, then each of the random processes can be constructed separately by using KLE [19]. However, if the random processes are correlated in time and/or spatial domains, then the random processes cannot be straightforwardly expanded separately. Thus, it is necessary to develop appropriate methods to effectively simulate the correlated random processes. The probabilistic principal component analysis [20,21] has been proposed to represent the correlated processes, which expands the correlated random processes in terms of a linear combination of independent random variables. In this method, all of the random variables representing the random processes are assumed to be independent; therefore it cannot properly represent cross-correlated random processes [22,23]. Another technique that has been proposed to represent correlated nonstationary processes is the spectral density method [24,25]. This method provides good results in capturing the autopower spectral density and the cross-power spectral density [26]. However, it is limited to stationary random processes, and only spatial correlation of random processes can be considered. An

algorithm that relies on expansions in terms of correlated sets of random variables reflecting the cross-covariance structure of the processes has also been proposed [23].

A linear nonstationary random vibration analysis of the complex system for uncorrelated and correlated random processes has been conducted in authors' previous works [1,17,18]. To develop a method suitable for nonlinear random vibration analysis under nonstationary random excitation, with correlation in both time and space, an algorithm that integrates Karhunen-Loeve expansion (KLE), nonlinear finite element method (NFEM), and a sampling technique for performing Monte-Carlo simulation is proposed. The outline of this work is as follows: in Sec. II, the theory of Karhunen-Loeve expansion for correlated random processes is addressed. Then an algorithm is proposed for nonlinear random vibration analysis of complex structures under multicorrelated random excitations. In Secs. III and IV, the proposed methodology algorithm is applied to rigid and flexible aircraft wings subjected to both stationary and nonstationary correlated excitations. Finally, conclusions are drawn in the last section.

II. Nonstationary Random Vibration Analysis of Systems with Geometric Nonlinearity

A. Karhunen-Loeve Expansion for Multiple Correlated Processes

A time-invariant second-order system with geometric nonlinearity subjected to a forcing function can be written as:

$$M\ddot{x} + C\dot{x} + Kx + H(x)x = f(t, \omega) \quad (1)$$

where M and C are mass and damping matrix of the system, K is the linear elastic stiffness matrix, $H(x)$ is the generalized unsymmetrical nonlinear stiffness matrix, $f(t, \omega)$ are the individual excitation component function of random forces whose components are $f_i(t, \omega)$, and ω is the sample space of the random excitations. Typically, long-aspect-ratio beams and wings excited by gust can be represented by Eq. (1). If the excitations are the distributed random forces $F(t, \omega)$, then the distributed forces can be converted into discrete forces $f(t, \omega)$ as [27,28]:

$$f(t, \omega) = \sum_{j=1}^{NE} T \int_A NF(t, \omega) dA \quad (2)$$

where, NE is the element number, T is the transfer matrix that transforms element coordinates to global coordinates, N is the shape functions of the system, A is the area over which the force is applied.

In many engineering problems, the material properties and/or forces are described as random quantities, and they are also functions of time or spatial dimensions. In this case, it is necessary to consider joint probability density functions for the material properties and/or forces. Nevertheless, this description becomes cumbersome when the responses of the system are calculated using the joint distribution of many random variables. Hence, it is advantageous to study the interaction among multiple random processes and extract as much information as possible from that relationship [8]. The relationship among multirandom variables is achieved through covariance and correlation analysis. Here, the forcing function $f_i(t, \omega)$ is prescribed by their autocovariance functions and mean values, which can range from a stationary to a nonstationary process, a Gaussian to a non-Gaussian process, a narrowband random process to a broadband one.

Let us consider an ensemble of square integrable random processes $f_i(t, \omega)$. The covariance of random processes, $f_i(s, \omega)$ and $f_j(t, \omega)$ with mean values μ_i and μ_j , is given as:

$$C_{F_i F_j}(s, t) = E[(f_i(s, \omega) - \mu_i)(f_j(t, \omega) - \mu_j)] \quad (3)$$

where $E[\]$ denotes the statistical expectation operator. If a process $f_i^*(t, \omega)$ is substituted for $f_j(t, \omega)$ in Eq. (3), where $f_i^*(t, \omega)$ is simply a time-shifted version of $f_i(s, \omega)$, then Eq. (3) is known as autocovariance $C_{F_i F_i}(s, t)$.

The KLE provides a way to discretize the autocovariance function of excitation such that it can be used to carry out the random vibration analysis [29]. If the random processes $f_i(t, \omega)$ are uncorrelated, then the KLE can be applied to each process that can be constructed separately [19]. However, if the random processes $f_i(t, \omega)$ are correlated, that is, if the cross-covariance functions are nonzero, then the random processes cannot be straightforwardly expanded into consistent expansions. Using KLE, the correlated random processes is written as a combination of the mean forcing component and the random orthogonal components:

$$f_i(t, \omega) = \mu_F^{(i)}(t) + \sum_{k=1}^n \sqrt{\lambda_k^{(i)}} \phi_k^{(i)}(t) \xi_k^{(i)}(\omega) \quad (4)$$

where $\lambda_k^{(i)}$ and $\phi_k^{(i)}(t)$ are, respectively, the eigenvalues and corresponding eigenfunctions of the autocovariance function $C_{F_i F_i}(s, t)$; $\xi_k^{(i)}(\omega)$ represent sets of correlated random variables, which will be discussed in Sec. II.B; and n is the truncated number of KLE terms and strongly depends on the desired accuracy and the autocovariance function of the stochastic field. Because the eigenvalues $\lambda_k^{(i)}$ decay monotonically with increasing values of its index, an appropriate measure of KLE truncation error is given as [23]:

$$\text{err} = \left(\sum_{k=1}^N \lambda_k - \sum_{k=1}^n \lambda_k \right) / \sum_{k=1}^N \lambda_k \quad N > n \quad (5)$$

The eigenvalues $\lambda_k^{(i)}$ and corresponding eigenfunctions $\phi_k^{(i)}(t)$ of the autocovariance function are found by solving a Fredholm equation of the second kind [29]:

$$\int_{t_{\min}}^{t_{\max}} C_{F_i F_i}(t_1, t_2) \phi_k^{(i)}(t_1) dt_1 = \lambda_k^{(i)} \phi_k^{(i)}(t_2) \quad (6)$$

where t_{\min} and t_{\max} are the initial and final times.

Here, sets of orthogonal basis functions are employed to solve the Eq. (6). The eigenfunctions $\phi_k^{(i)}(t)$ can be further expanded as:

$$\phi_k^{(i)}(t) = \sum_{j=1}^n d_{jk}^{(i)} h_j^{(i)}(t) \quad (7)$$

where $d_{jk}^{(i)}$ are basis function participation factors and $h_j^{(i)}(t)$ are user-defined basis functions. From our previous research [1,17,18] experience, simple piecewise constants are adopted as the basis functions.

The result of solving Eq. (6) using user-defined basis functions is a classical matrix eigenvalue problem, as shown in Eq. (8).

$$\mathbf{GD} = \mathbf{\Lambda QD} \quad (8)$$

where

$$G_{ij} = \int_{t_{\min}}^{t_{\max}} \int_{t_{\min}}^{t_{\max}} C_{F_i F_i}(t_1, t_2) h_i(t_2) h_j(t_1) dt_1 dt_2 \quad (9)$$

$$Q_{ij} = \int_{t_{\min}}^{t_{\max}} h_i(t) h_j(t) dt \quad (10)$$

$$\mathbf{\Lambda}_{km}^{(i)} = \delta_{km} \lambda_k^{(i)} \quad (11)$$

Construction of the N matrix is very similar to that for a typical Galerkin-type problem. Once the eigensystem of Eq. (8) is solved, the eigenfunctions must be scaled appropriately. The MATLAB eigensystem solver typically scales the eigenvectors such that their L_2 norm is equal to unity. While this is appropriate for many applications, it is not, in this case, as the magnitude of the eigenvector plays an integral role in the calculation of the response using KLE [30]. An appropriate way of scaling can be obtained by making use of the Fredholm Eq. (6). The computed eigenvalues $\lambda_k^{(i)}$ and

eigenfunctions $\phi_k^{(i)}(t)$ are substituted back into the Fredholm equation and compare the values for the left- and right-hand side of the Eq. (6). Then, a scaling factor can be found using this method, which is then applied to the eigenvector under study. The left- and right-hand side of the Fredholm equation is checked once more with the scaled eigenvalues and eigenfunctions to ensure that a correct scaling factor has been used.

B. Correlated Random Variables for Multicorrelated Processes

By definition, the correlation of random variables shown in Eq. (4) are as follows:

$$P_{km}^{(ij)} = E[\xi_k^{(i)} \xi_m^{(j)}] \quad (12)$$

If the random processes are correlated only in the time domain, the cross-covariance functions only depend on time parameters s and t . If the random processes have a correlation in both time and space domain, the cross-covariance functions depend on not only the time parameters s and t but also spatial parameters l_1 and l_2 . When using the definition of correlation in Eq. (12) and the KLE, the cross-covariance functions can be obtained for the zero mean random variables as follows:

$$C_{F_i F_j}(s, t, l_1, l_2) = E[f_i(s, \omega) f_j(t, \omega)] \\ = \sum_{k=1}^n \sum_{m=1}^n P_{km}^{(ij)}(l_1, l_2) \sqrt{\lambda_k^{(i)} \lambda_m^{(j)}} \phi_k^{(i)}(s) \phi_m^{(j)}(t) \quad (13)$$

The correlation of random variables $P_{km}^{(ij)}$ in Eq. (12) can be determined by projecting the kernels $C_{F_i F_j}(s, t)$ onto the eigenfunction set of each random process, which yields [23,31]:

$$P_{km}^{(ij)}(l_1, l_2) = \frac{1}{\sqrt{\lambda_k^{(i)} \lambda_m^{(j)}}} \int_0^T \int_0^T C_{F_i F_j}(s, t, l_1, l_2) \phi_k^{(i)}(s) \phi_m^{(j)}(t) ds dt \quad (14)$$

Let \mathbf{P} be the block matrix

$$\mathbf{P} = \begin{bmatrix} \mathbf{I} & P^{12} & \dots & P^{1n} \\ P^{21} & \mathbf{I} & \dots & P^{2n} \\ \vdots & \vdots & \ddots & \vdots \\ P^{n1} & P^{n2} & \vdots & \mathbf{I} \end{bmatrix} \quad (15)$$

where \mathbf{I} is the identity matrix and P^{ij} is the matrix defined in Eq. (14). Note that \mathbf{P} is asymmetric and may not be necessarily positive definite.

The correlated random variables $\xi_k^{(i)}(\omega)$ in Eq. (4) can be obtained from a transformation of uncorrelated random variables. Let

$$\xi_k^{(i)} = \begin{bmatrix} \{\xi_k^{(1)}(\omega)\} \\ \{\xi_k^{(2)}(\omega)\} \\ \vdots \\ \{\xi_k^{(n)}(\omega)\} \end{bmatrix} \quad (16)$$

be a jointly normally distributed random vector with correlation matrix \mathbf{P} and can be obtained as follows [23]:

$$\xi = \boldsymbol{\varphi} \boldsymbol{\zeta} \sqrt{\boldsymbol{\gamma}} \quad (17)$$

where $\boldsymbol{\zeta}$ is a vector of independent standard Gaussian random variables with a mean value equal to zero and a variance equal to one, which can be obtained by using Latin Hypercube Sampling (LHS). Here, $\boldsymbol{\varphi}$ and $\boldsymbol{\gamma}$ are eigenvalues and eigenvectors of the correlation matrix \mathbf{P} .

C. Response of System with Geometric Nonlinearity Under Multicorrelated Random Excitations

Using the definition of KLE of the forcing function as given in Eq. (4), Eq. (1) is written as:

$$\mathbf{M}\ddot{\mathbf{x}} + \mathbf{C}\dot{\mathbf{x}} + \mathbf{K}\mathbf{x} + \mathbf{H}(\mathbf{x})\mathbf{x} = \mu_F(t) + \sum_{k=1}^n \sqrt{\lambda_k} \phi_k(t) \xi_k(\omega) \quad (18)$$

The response of the system $x_i(t)$ with geometric nonlinearity due to correlated random processes $f_i(t, \omega)$ can be obtained by using a sampling technique and nonlinear finite element method, which is a more generic approach for large and complex systems as compared with the analytical approach. First, the correlated excitations are obtained by using sampling techniques. Then the nonlinear analysis due to the correlated excitations is carried out by using MSC.NASTRAN solution 400 or 600. MSC.NASTRAN implements the nonlinear analysis by offering several stiffness update strategies, such as full Newton-Raphson, modified Newton-Raphson, strain correction method, and a Secant procedure [32]. The full Newton-Raphson method updates the tangent stiffness matrix once per increment, which provides excellent results for most nonlinear problems. The modified Newton-Raphson method is similar to the full Newton-Raphson method but does not formulate and factor the tangent stiffness matrix in each iteration. The strain correction method is a variant of the full Newton method, which uses a linearized strain calculation, with the nonlinear portion of the strain increment applied as an initial strain increment in subsequent iterations and recycles. This method is appropriate for shell, plate, and beam problems in which rotations are large, but membrane stresses are small. The Secant method is based on the Davidon-rank one, quasi-Newton update. The Secant method is similar to the modified Newton-Raphson method in that the stiffness matrix is calculated only once per increment. In this research, the full Newton-Raphson was selected in MSC.NASTRAN solution sequence SOL 400 to solve the geometric nonlinear problem.

Then the autocovariance $R_{X_i X_i}(t_1, t_2)$ and variance $\sigma_{X_i X_i}^2(t)$ of the response are represented as:

$$R_{X_i X_i}(t_1, t_2) = E[x_i(t_1), x_i(t_2)] \quad (19)$$

$$\sigma_{X_i X_i}^2(t) = E[x_i(t), x_i(t)] \quad (20)$$

D. Implementation Procedure for Random Vibration Analysis

An algorithm is proposed to carry out nonstationary random vibration analysis of the systems with geometric nonlinearity under multiple random excitations that are correlated both in time and space. The implementation procedure is as follows:

- 1) Define the geometry and material properties of the structure.
- 2) Define or obtain the autocovariance function $C_{F_i F_i}$ and cross-covariance function $C_{F_i F_j}$ of excitation.
- 3) Choose the piecewise constant function as the basis function, and then the eigenvalues $\lambda_k^{(i)}$ and eigenfunctions $\phi_k^{(i)}$ of autocovariance function $C_{F_i F_i}$ are obtained by solving a Fredholm equation of the second kind.
- 4) Correlation matrix \mathbf{P} of random processes is calculated by Eqs. (14) and (15), and then the eigenvalues γ_i and eigenvectors φ_i of correlation matrix \mathbf{P} are obtained.
- 5) The correlated random variables $\xi_k^{(i)}$ are obtained by Eq. (17).
- 6) Using the eigenvalues $\lambda_k^{(i)}$ and eigenfunctions $\phi_k^{(i)}$ of autocovariance function in Step 3 and the correlated random variables $\xi_k^{(i)}$ in Step 5, the correlated random excitations $f_j(t, \omega)$ are obtained by KLE.
- 7) Create the finite element model of structure, and the correlated excitations $f_j(t, \omega)$ are applied.
- 8) The nonlinear response analysis is carried out by using nonlinear finite element method and sampling technique.

III. Application to a Rigid Aircraft Wing

To verify the accuracy of the proposed algorithm under correlated nonstationary excitation, the method is applied to an aircraft wing that is simplified as a rigid system where the effect of the mass of the aircraft and aerodynamics due to gust are considered. The effect of the flexibility of the structures is ignored to derive the approximate acceleration and vertical velocities of the wing due to the gust. But the effect of spatial distribution (in the plane of the wing) of the vertical gust is accounted for the rigid wing. Such simplifications are commonly made at the preliminary design stage even for large flight vehicles. Traditionally, the rigid-wing is modeled as a 2-D airfoil, and hence the cross-correlation effects of the excitations are neglected. The nonstationary analysis of a wing as a rigid 2-D plane element will verify the applicability of the proposed methodology with the analytical results published earlier [33,34] along with studying the effects of cross-correlation effects of the excitations. The plunging rigid body motion of the rigid aircraft wing is only considered, and the effect of geometric nonlinearity cannot be taken into account in this case. The rigid aircraft wing model is shown in Fig. 1 and the dimensions and physical properties are given in Table 1. Here, the response of the wing as the free-free structure is studied.

Vibration generated by gust excitation has been and continue to be of interest in the design of aircraft [35,36]. In this work, the excitation is due to the gust caused by the differential heating of the earth's atmosphere by the Sun [37]. Gust loads are a great concern to an aircraft designer because of gusts' influence on the ride quality, safety, and for the long-term due to the fatigue life of the aircraft and in view of the control upset problem on the safety. It has been verified experimentally [33] that the gust velocity is approximately Gaussian distributed. However, strong nonstationary characteristics are also evident in some cases, especially, for low-altitude turbulence over rough terrain. Thus, random vibration analyses of the rigid aircraft wing excited by stationary and nonstationary gusts are carried out. Here, the gust only in the vertical direction is considered.

A. Stationary Random Excitation

For the stationary gust excitation, significant research has been conducted previously to describe the characteristics of the gust. The Dryden model is one of most representative models that describe the stationary gust random excitation. The expression for the power spectral density (PSD) function of the gust velocity is given as [33]:

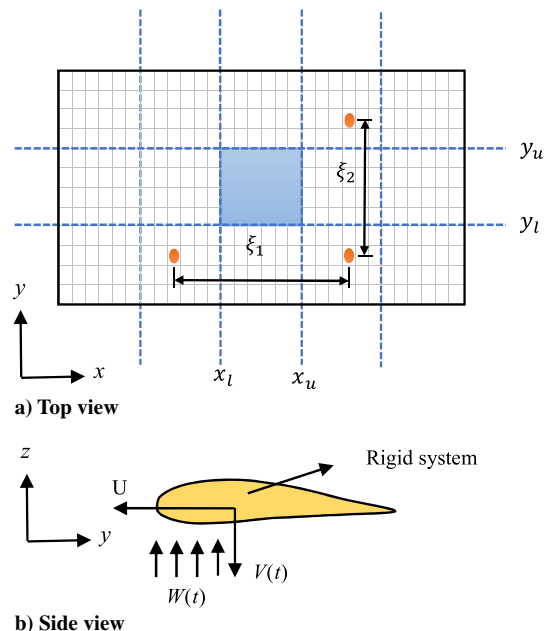


Fig. 1 The rigid aircraft wing excited by gust.

Table 1 Rigid aircraft wing dimensions and physical properties

Parameters	Values
Full span	50 m
Aspect ratio	5
Mass parameter (a)	1.12
Lift curve slope	2π

$$S_{F_i F_i}(\omega) = \frac{\sigma^2 B}{2\pi U} \left[\frac{1 + (3\omega B/U)^2}{1 + (\omega B/U)^2} \right] \quad (21)$$

where σ^2 represents the variance of the gust velocity, B is the turbulence length scale, and U is the aircraft speed. Then an approximate autocovariance of the gust can be obtained by a transfer function representation of the Dryden PSD function as in Eq. (22) and is shown in Fig. 2.

$$C_{F_i F_i}(t_1, t_2) = \sigma_i^2 \left(1 - \frac{|t_1 - t_2|}{2\tau_i} \right) \exp\left(-\frac{|t_1 - t_2|}{\tau_i}\right) \quad (22)$$

where τ_i represents the autocorrelation length, and $\tau_i = B/U$.

As the gust excitations are correlated both in time and space, the gust profiles along the streamwise and spanwise directions are assumed to be of the form of an exponential correlation. Then, the cross-covariance of the gust is obtained as follows:

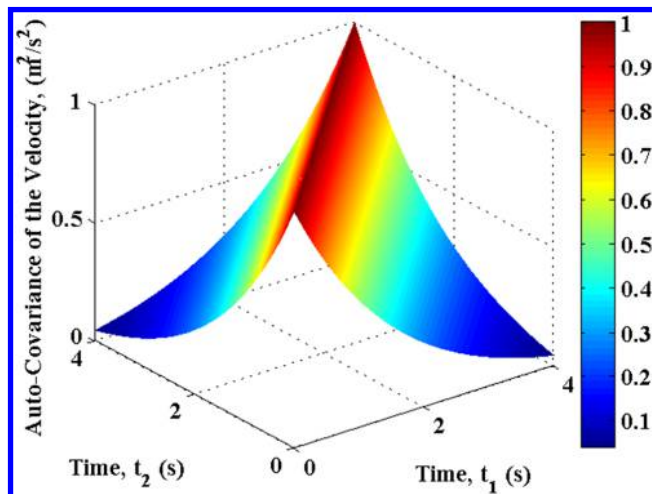
$$C_{F_i F_j}(\zeta_1, \zeta_2, t_1, t_2) = \frac{\sigma_i^2}{\tau_{ij}} \left(1 - \frac{|t_1 - t_2|}{2\tau_{ij}} \right) \exp\left(-\frac{|t_1 - t_2|}{\tau_{ij}}\right) \times \exp\left(-\gamma_1 \left| \frac{\zeta_1}{U} \right| \right) \exp\left(-\gamma_2 \left| \frac{\zeta_2}{U} \right| \right) \quad (23)$$

where ζ_1 and ζ_2 are the separation distances in the streamwise and spanwise directions, γ_1 and γ_2 are the decay rates, and τ_{ij} is the cross-correlation length.

According to the KLE of the gust autocovariance, the gust velocity $W(t)$ can be first obtained. Then the vertical velocity $V(t)$ and acceleration $\dot{V}(t)$ of the rigid wing as shown in Fig. 1 can be calculated by using the quasi-steady state aerodynamics theory as follows [37]:

$$\dot{V}(t) + aV(t) = -aW(t) \quad (24)$$

where $a = \rho US(dC_L/d\alpha)/2M$ is the mass parameter of the aircraft, ρ is the density of air, S is the area of the wing, M is the half mass of the aircraft, and $dC_L/d\alpha$ is the lift curve slope. The pressure applied to wing due to gust can be obtained by using Eq. (24) as follows:

**Fig. 2 Autocovariance function of stationary gust excitation.****Table 2 Numerical values of the parameters used in the gust model**

Parameters	Values
Aircraft velocity (U)	60.96 m/s
Turbulence length scale (B)	152.4 m
Density of air (ρ)	1.21 kg/m ³
Decay rate, streamwise (γ_1)	0.16
Decay rate, spanwise (γ_2)	0.46
Variance of the gust velocity (σ^2)	0.81 m ² /s ²
Autocorrelation length (τ_i)	2.5
Cross-correlation length (τ_{ii})	2.5

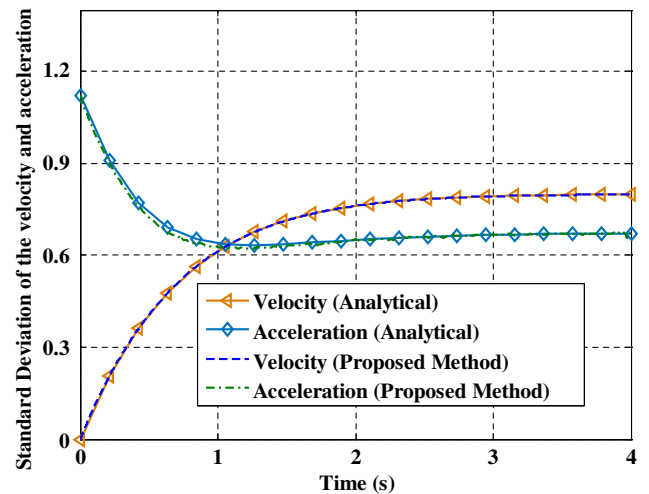
$$P(t) = \frac{1}{2} \rho U \frac{dC_L}{d\alpha} [W(t) + V(t)] \quad (25)$$

The parameters of the stationary gust excitation used in this manuscript are taken from [37] and given in Table 2.

The standard deviations of vertical velocity and acceleration are obtained by the proposed method and compared with the analytical results given by Lee [34] as shown in Fig. 3. The results obtained by proposed method have an excellent agreement with the analytical results, which means that the proposed algorithm and the obtained results are feasible, correct, and valid.

For the random vibration analysis, the amount of computing data would become very significant if we consider correlation in both the time and space domains. Therefore, to capture the spatial correlation efficiently, the wing is divided into several subdomains, as shown in Fig. 1; for example, x_l , x_u , y_l , and y_u are the bounds of a subdomain. Subscripts l and u on x and y are used for the lower and upper bounds in the x and y directions, respectively. However, the process of partitioning the domain cannot be completely arbitrary. The division of subdomains must be fine enough to obtain accurate results. To find an optimal number of subdomains, the wing is divided into different subdomains, varying from 1×1 to 6×3 grid. The standard deviations of the velocities with different subdomains are shown in Fig. 4. Results show that the standard deviations of the velocity of the wing converge to a relatively stable value with an increase in the number of subdomains. Therefore, the number 6×3 grid is determined to be sufficient for the random vibration analysis.

The effect of correlation among random excitations on the structural response is also studied. The structural responses are calculated using three different excitations: 1) perfectly correlated excitations where the correlation between the random processes is one, 2) uncorrelated excitations where the correlation between the random processes is zero, and 3) partially correlated excitations

**Fig. 3 Results using analytical and proposed method under stationary excitation.**

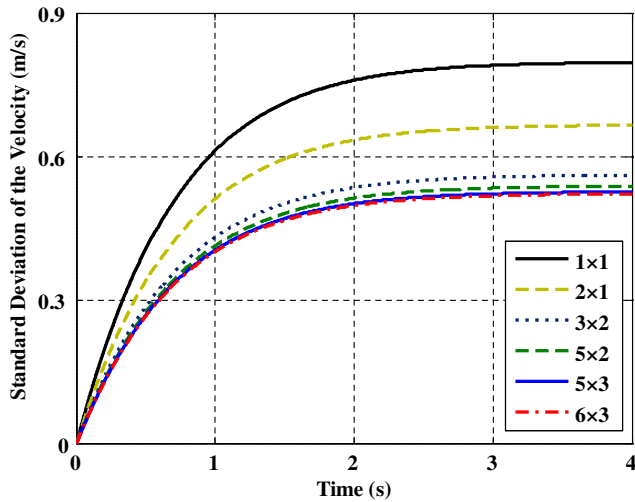


Fig. 4 Results with different number of subdomains under partially correlated stationary excitation.

where the correlation between the random processes is defined by Eq. (14). The standard deviations of the velocity and acceleration with different correlations are obtained and shown in Fig. 5. The corresponding covariances of the velocity and acceleration under partially correlated excitation are presented in Fig. 6. Results indicate that the response due to partially correlated random excitation is bounded by the responses obtained by perfectly correlated and uncorrelated random process excitations. The changes of response

may be attributable to the phase difference between different excitation locations of the system. The additional effect produced by phase difference is ignored in the uncorrelated case. When the excitations are treated as perfectly correlated, the response increases due to some overlap of excitation that is caused by correlation.

B. Nonstationary Random Excitation

The nonstationary character of the gust has led to an increasing use of nonstationary models in performing response analysis of aircraft due to gusts. A convenient and realistic way of representing the nonstationary character of the gust velocity is to model it in a uniformly modulated form given by:

$$W(t) = r(t)G(t) \quad (26)$$

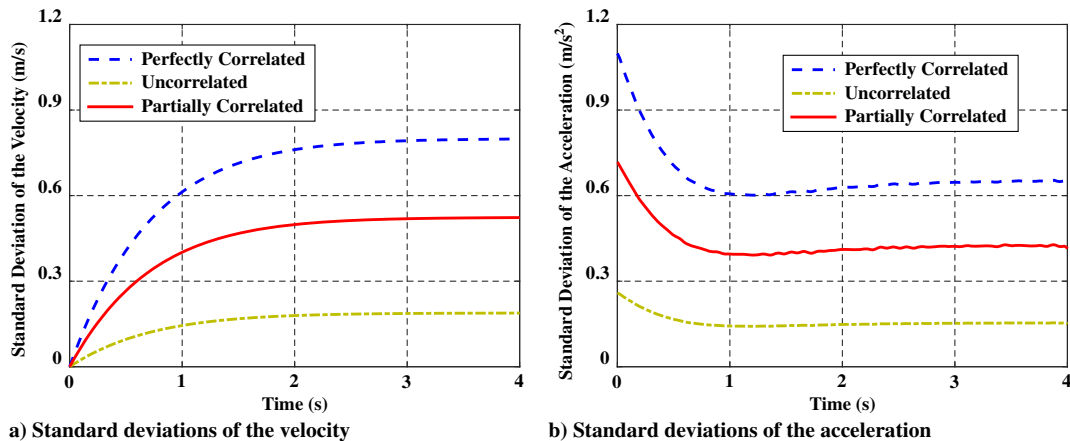
where $G(t)$ is a zero-mean stationary Gaussian random process and $r(t)$ is a deterministic function of time. Howell and Lin [33] assumed the modulating function $r(t)$ to be of the form:

$$r(t) = c(e^{-\alpha t} - e^{-\beta t}) \quad (27)$$

where $\beta > \alpha > 0$ and $c > 0$. The α , β , and c are constant and can be selected so as to make the resulting profile to resemble rather well with the atmosphere gust profile.

Equation (26) can be further expressed into a Fourier Stieltjes integral as:

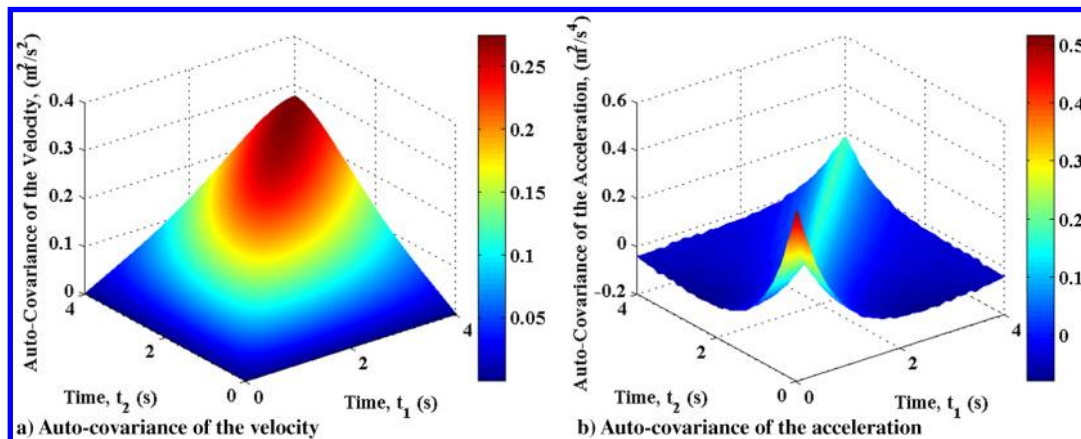
$$W(t) = \int_{-\infty}^{\infty} r(t)e^{i\omega t} d\tilde{G}(\omega) \quad (28)$$



a) Standard deviations of the velocity

b) Standard deviations of the acceleration

Fig. 5 Results under perfectly correlated, uncorrelated, and partially correlated stationary excitations.



a) Auto-covariance of the velocity

b) Auto-covariance of the acceleration

Fig. 6 Results under partially correlated stationary excitation.

where $\tilde{G}(\omega)$ is an orthogonal random process with [37]:

$$\begin{aligned} E\left[d\tilde{G}(\omega_1)d\tilde{G}(\omega_2)\right] &= 0 & \omega_1 \neq \omega_2 \\ E\left[|d\tilde{G}(\omega)|^2\right] &= S_{F_i F_i}(\omega)d\omega & \omega_1 = \omega_2 \end{aligned} \quad (29)$$

Then the autocovariance function of the gust can be obtained using the evolutionary spectral analysis as:

$$C_{F_i F_i}(t_1, t_2) = \int_{-\infty}^{\infty} r(t_1)r(t_2)e^{i\omega(t_1-t_2)} S_{F_i F_i}(\omega) d\omega \quad (30)$$

Substituting Eqs. (21) and (27) into Eq. (30), the autocovariance of the nonstationary gust is derived as follows:

$$\begin{aligned} C_{F_i F_i}(t_1, t_2) &= c^2 \sigma_{ij}^2 \left[e^{-\alpha(t_1+t_2)} + e^{-\beta(t_1+t_2)} - e^{-\alpha t_1 - \beta t_2} - e^{-\beta t_1 - \alpha t_2} \right] \\ &\times \left(1 - \frac{|t_1 - t_2|}{2\tau_{ij}} \right) \exp\left(-\frac{|t_1 - t_2|}{\tau_{ij}}\right) \end{aligned} \quad (31)$$

Similarly, as is done in the case of stationary covariance excitation, the correlation of gust along the streamwise and spanwise directions can be presented as an exponential decaying oscillating function. Then the cross-covariance of the nonstationary gust is as follows:

$$C_{F_i F_j}(\zeta_1, \zeta_2, t_1, t_2) = C_{F_i F_i}(t_1, t_2) \exp\left(-\gamma_1 \left| \frac{\zeta_1}{U} \right| \right) \exp\left(-\gamma_2 \left| \frac{\zeta_2}{U} \right| \right) \quad (32)$$

The parameters of the nonstationary gust excitation used in this paper are given in Table 2, and the autocovariance of the nonstationary gust excitation is shown in Fig. 7.

The standard deviations of the acceleration obtained by the proposed method under nonstationary gust with different values of β are obtained and compared with the analytical results conducted by Howell and Lin [33] as shown in Fig. 8. Here, the parameters α and c are set equal to 0 and 1, respectively. The results obtained by the proposed method have an excellent agreement with the analytical results for all values of β . It can also be observed that the structural responses for all values of β tend to become stationary random processes with time. It is because the excitation tends to be a stationary random process with the increase of time. However, in a stationary analysis, the transient overload is not detected. We can also see that the responses become more and more pronounced as the increment of β . The parameter β has a significant effect on the structural response. Therefore, the parameter β should be set carefully in an actual situation, and it can usually be obtained through experiments. The parameter β is set equal to 5 in the following analysis.

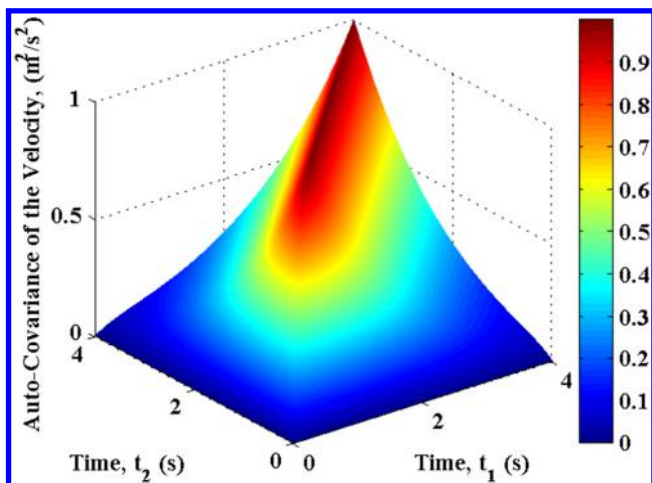


Fig. 7 Nonstationary autocovariance function of gust excitation.

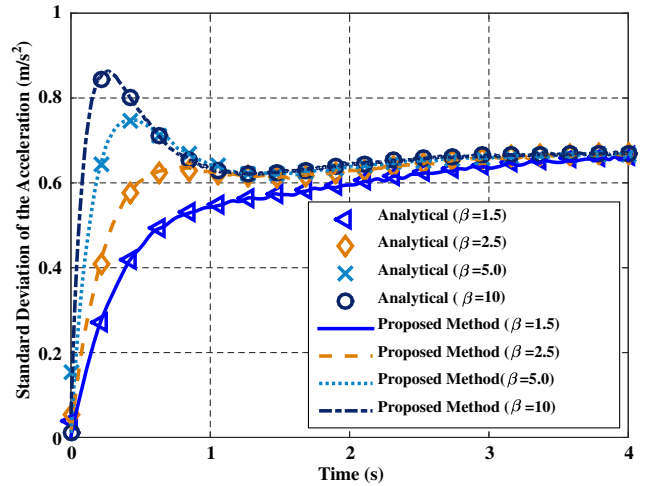


Fig. 8 Results using analytical and proposed method under nonstationary gust.

The convergence of the structural responses under nonstationary gust with a different number of subdomains is also studied, as shown in Fig. 9. Results indicate that the responses converge to a relatively stable value with the increase of the subdomains' number. Therefore, for the nonstationary gust excitation, the number of subpanels (6×3) is also enough and reasonable to carry out the random vibration analysis. Then the effect of correlation between random excitations on the structural response is also studied. The standard deviations of the acceleration with different correlated excitations that are perfectly correlated, partially correlated, and uncorrelated excitations are shown in Fig. 10. The corresponding autocovariances of the acceleration under partially correlated excitation are plotted in Fig. 11. The results once again verify that the response will be larger for the perfectly correlated case and smaller for the uncorrelated case than that for the actual conditions.

IV. Application to a Flexible Aircraft Wing

To further demonstrate the general applicability of the proposed methodology, a complex structure, a flexible aircraft wing as shown in Fig. 12 is used in this research. The flexible wing is a subsonic wing, which is known as the NASA common research model (CRM) [38] wing. The wing consists of two wing sections: the inner wing and the outer wing, which are connected at the junction located at about 37% semispan. The front and the rear spars are located at 9% and 70%

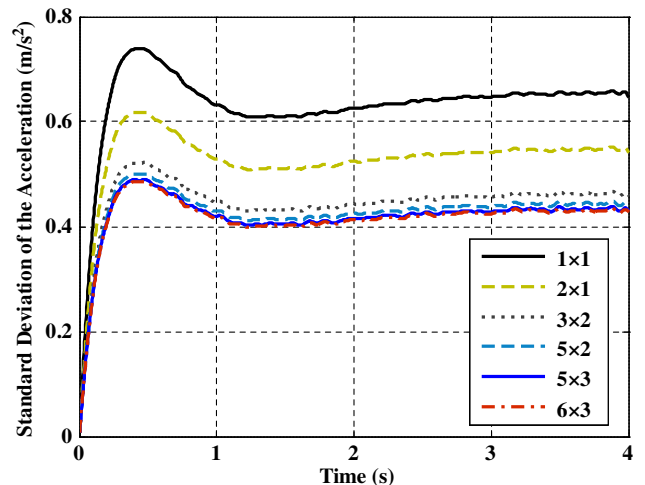


Fig. 9 Results with different number of subdomains under partially correlated nonstationary gust.

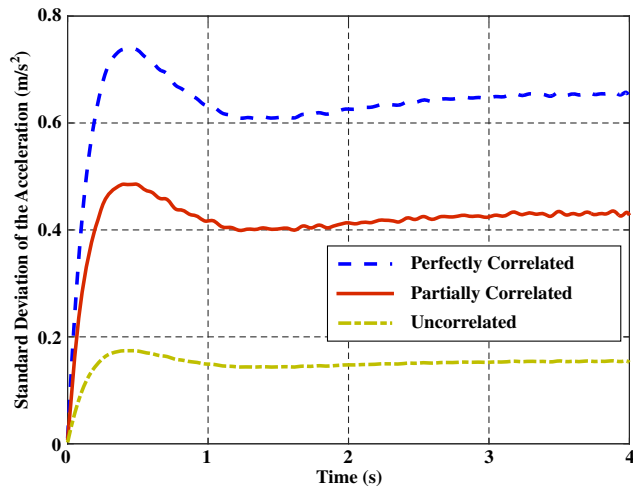


Fig. 10 Results under perfectly correlated, uncorrelated, and partially correlated nonstationary gusts.

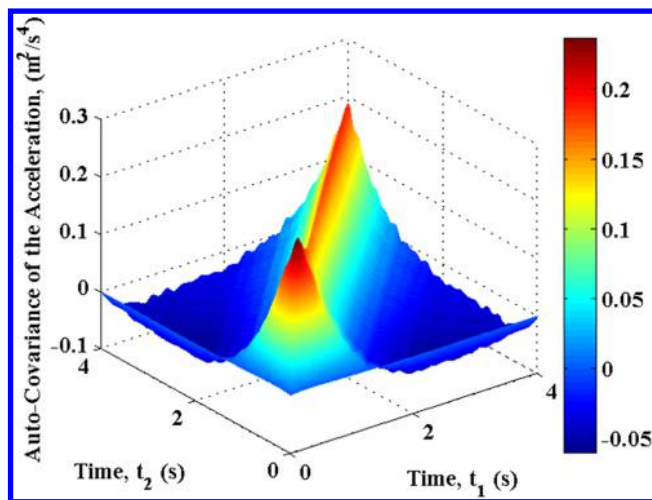


Fig. 11 Results under partially correlated nonstationary gust.

of the chord, respectively. The ribs are placed in the region between the front and rear spars. The wing is modeled using aluminum alloy 2024-T3, and its dimensions and material properties are given in Table 3.

The FEM of the CRM wing is modeled by using four-noded quadrilateral elements (CQUAD4 in Nastran), as shown in Fig. 12. In the FEM, it is important to study the convergence to estimate the number of elements. The wing is modeled by using 4142, 9540, and 31,140 elements, as shown in Table 4. When the number of finite elements is greater than 9540, converged results can be obtained. Based on a combination of computational efficiency and sufficient accuracy, this optimum number 9540 of finite elements is determined

Table 3 The dimensions and material properties of the flexible aircraft wing

Parameters	Values
Full span	58.75 m
Aspect ratio	9
Taper ratio	0.275
Density	2768 kg/m ³
Modulus of elasticity	73.09 GPa
Poisson ratio	0.33

for subsequent analysis. The convergence of the structural response due to a number of samples is also studied for both stationary and nonstationary gust. A set of 1000 samples of random variables where the confidence reaches 98.11% is also sufficient for the random analysis of the flexible wing.

During the analysis of this wing, the root of the wing is usually assumed to be fixed as shown in Fig. 13a, and thus only elastic deformation of the wing is taken into account. In an actual situation, the response of wing includes both the elastic deformation and rigid body motion, which can be used for comfort evaluation. In the linear vibration analysis, the response of the wing can be obtained by a linear superposition of elastic and rigid body deformations, but it is not valid in the nonlinear vibration analysis. To get the overall response, including both the rigid and elastic responses in the nonlinear analysis, the *large mass method* (LMM) is employed to carry out the random vibration analysis. The LMM is a modeling technique in which the user places an element with a large mass at the points of known acceleration or displacement [39,40]. In effect, this large mass acts as a constraint at the connected point/location. Then, a correspondingly large force is applied to the large mass to produce the desired motion. If the added mass element is sufficiently heavy, the reaction forces from the actual structure will not affect the input motions. MSC software recommends that the value of large mass is approximately 10^6 times the mass of the entire structure. In this work, the LMM is simulated by attaching a huge mass that is attached to the wing by using RBE2 elements, as shown in Fig. 13b. The large force given in Eq. (24) and the pressure given in Eq. (25) are, respectively, applied to the large mass and the wing skin, and then the nonlinear response can be obtained by using nonlinear finite element method (NFEM). The stationary and nonstationary gusts in this section are same as given in Sec. III. Two points, A and B, at the tip and the root of the wing, respectively, are selected for monitoring the random vibrations, as marked in Fig. 13.

To capture the spatial correlation of a gust, the wing is divided into several subdomains, as shown in Fig. 14. The convergence of the structural response by varying the number of subdomains is studied. The standard deviations of the acceleration at point A under stationary and nonstationary gusts with various number of subdomains are shown in Fig. 15. Results show that the number of subpanels (6×4) is enough and reasonable to carry out the random vibration analysis. The structural responses at point A due to the perfectly correlated, partially correlated, and uncorrelated stationary and nonstationary excitations are obtained as shown in Figs. 16 and 17. The standard deviation at the tip is becoming less oscillatory after 2 s, and the standard deviation of

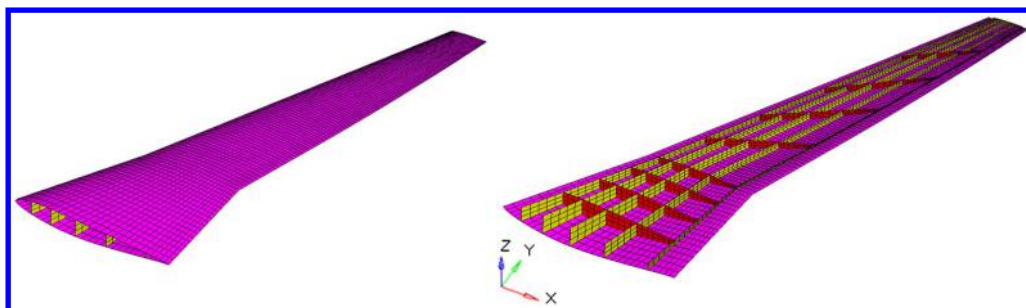


Fig. 12 The flexible aircraft wing model.

Table 4 The first 10 natural frequencies of the flexible aircraft wing (Hz)

Number of elements	1	2	3	4	5	6	7	8	9	10
4,142	1.54	5.51	8.91	11.05	11.23	12.60	12.85	13.09	13.65	13.97
9,540	1.27	4.90	8.32	10.36	10.58	11.05	11.44	11.70	12.06	12.18
31,140	1.26	4.87	8.27	10.08	10.31	10.85	11.18	11.56	11.92	12.07

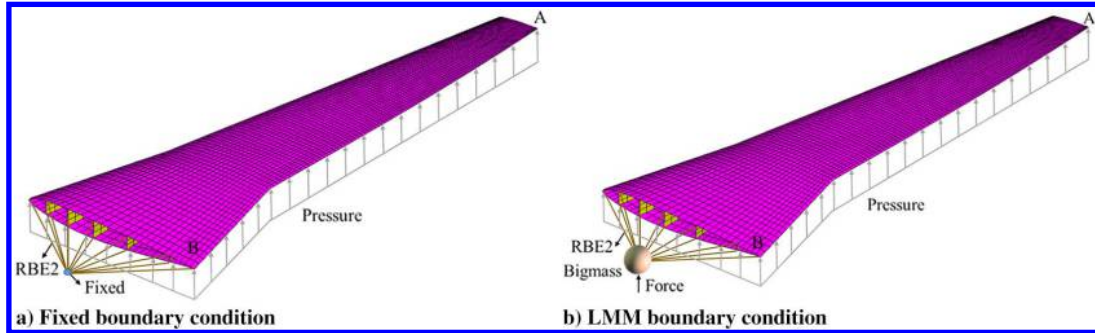


Fig. 13 The fixed and LMM boundary condition of the flexible aircraft wing.

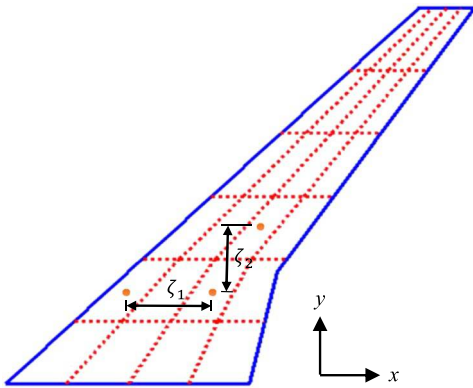


Fig. 14 Subdomains to capture the correlation on an aircraft wing.

displacement is becoming almost linearly increasing due to the modeling of the wing as a free-free structure will produce a rigid motion. The same conclusion as obtained in Sec. III is confirmed again that the structural responses due to correlated random processes are bounded by the response achieved by both perfectly correlated and uncorrelated random excitations.

Theoretically, the more samples of random variables are used in the sampling technique, the more accurate results will be obtained. Here,

LHS [41] is used to generate samples. However, the computational cost will be too high if one uses a large number of samples to carry out the random vibration analysis, especially for the case of nonlinear vibration. It is necessary to obtain an optimum number of samples based on computational efficiency and sufficient accuracy. To find this optimal number, the stationary and nonstationary nonlinear random vibration analyses are carried out by using 200, 400, 600, 800, and 1000 samples of random variables. The confidence levels with different values of sampling numbers are shown in Table 5, where the confidence interval is 95%. Results demonstrate that the confidence increases with an increase in the number of samples, and it reaches 98.11% when 1000 samples are used. Thus, a set of 1000 samples of random variables is sufficient for this problem.

To study the effect of geometric nonlinearity on the structural response, the standard deviations of displacement and acceleration at point A obtained using nonlinear analysis due to LMM and fixed boundary conditions are calculated and compared with the linear case results, as shown in Figs. 18 and 19, respectively. Results show that the geometric nonlinear effect has a hardening effect on this wing's response and results in a less oscillatory response amplitude compared with the linear case. Moreover, the geometric nonlinear effect results in stiffening of the aircraft wing, which decreases the wing's response. This is because a large out-of-plane deformation of the wing results in in-plane stretching, which in turn leads to a hardening of the wing. However, it is worth noticing that the effect of nonlinear stiffness matrix is not always stiffening. It may also have an

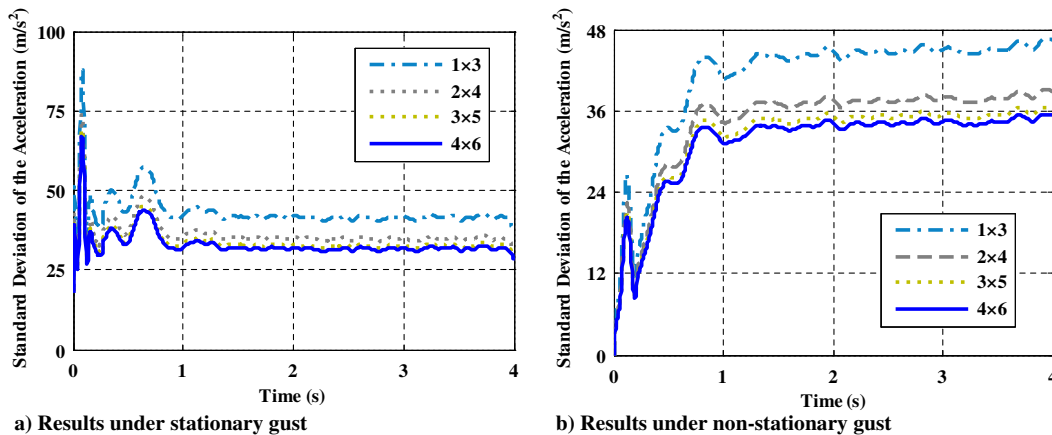


Fig. 15 Results with different number of subdomains under stationary and nonstationary gust.

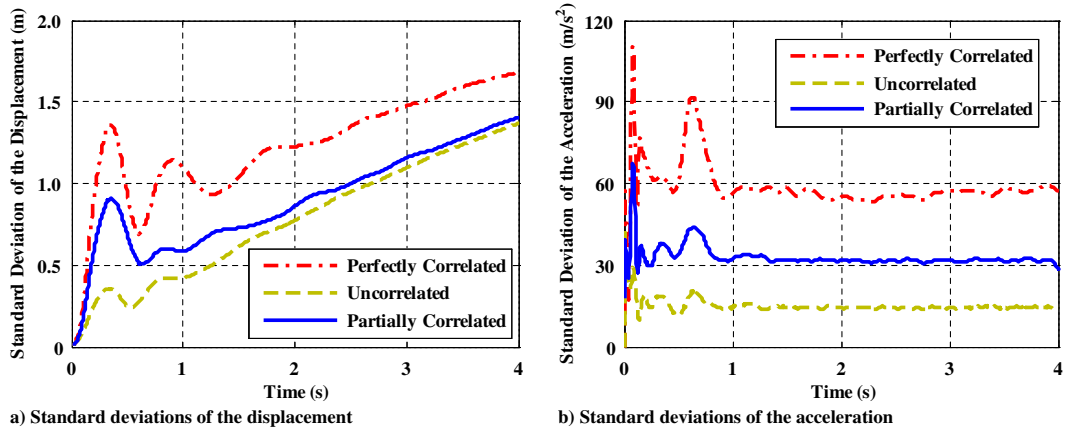


Fig. 16 Results under perfectly correlated, uncorrelated, and partially correlated stationary gust.

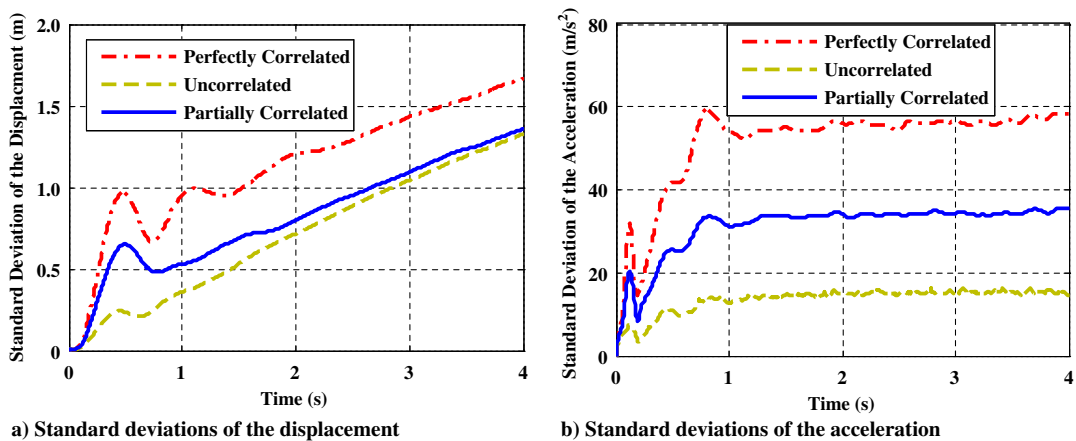


Fig. 17 Results under perfectly correlated, uncorrelated, and partially correlated nonstationary gust.

Table 5 Confidence levels with different sampling numbers when confidence interval is 95%

Sampling number	Confidence level, %
200	71.73
400	86.58
600	93.21
800	96.45
1000	98.11

adverse effect, and it depends on the type of boundary condition, the magnitude of excitation, and the nature of structural nonlinearity.

To study the nonlinear effect on the PDFs of response, the PDFs of linear and nonlinear displacements at point A at 1 s and 3 s using LMM boundary condition are obtained as shown in Fig. 20. All the PDFs of displacement are Gaussian for the linear system because the excitations expanded by KLE are Gaussian. However, in the nonlinear system, the PDFs of displacement are non-Gaussian even if the excitations are Gaussian. Meanwhile, the PDFs of displacement change over time, meaning that the distribution of the response is not

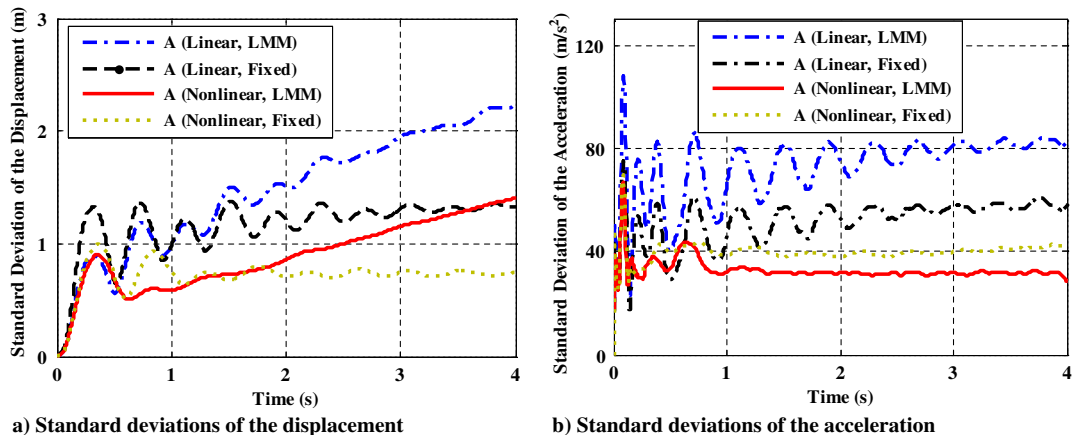


Fig. 18 Linear and nonlinear responses under stationary gust.

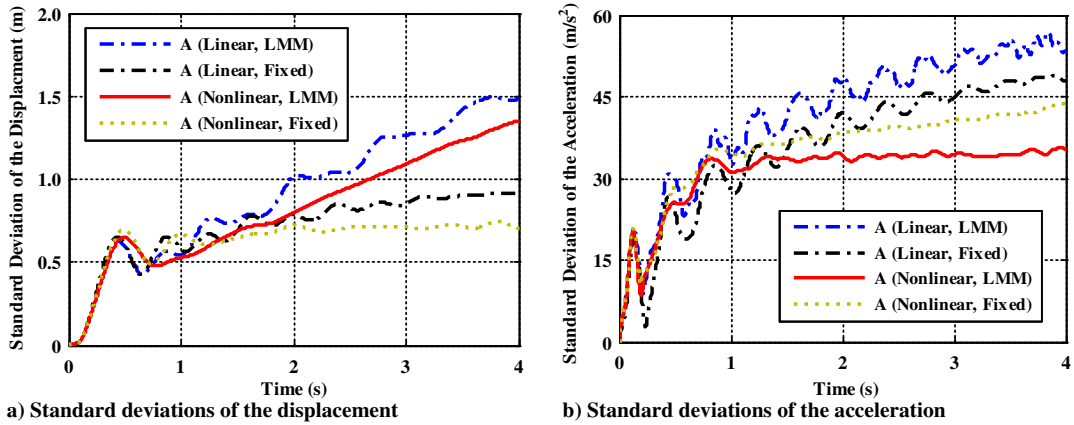


Fig. 19 Linear and nonlinear responses under nonstationary gust.

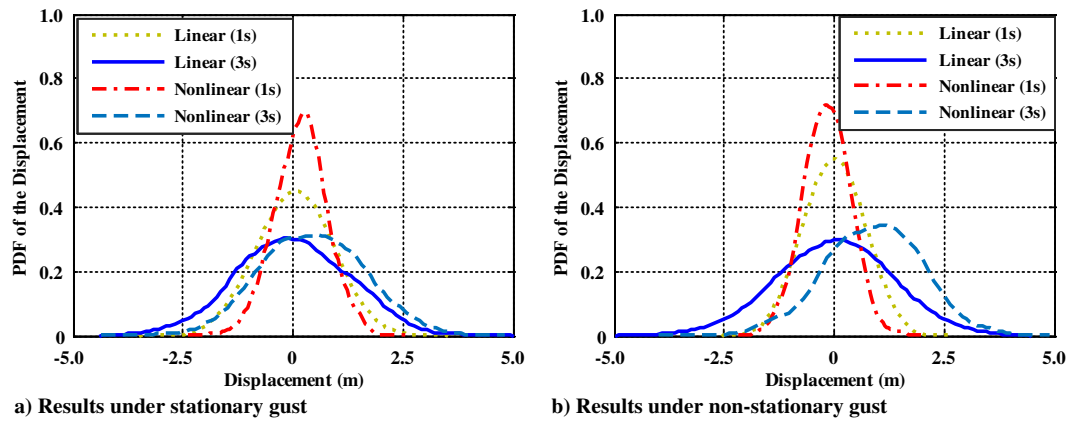


Fig. 20 PDFs of displacements under stationary and nonstationary gust.

fixed for a nonlinear system. Therefore, it is necessary to consider geometric nonlinearity of the systems while studying the dynamic vibration analyses; otherwise, it will result in inaccurate results.

To investigate the effect of boundary condition on the structural response, the random vibration analysis is carried out using two different boundary conditions: 1) LMM boundary condition and 2) fixed boundary condition. The elastic deformations of the wing in both LMM and fixed boundary conditions are calculated and compared. The elastic deformations using LMM boundary condition can be obtained by subtracting the responses at point B from the responses at point A, and then compared with the elastic deformations at point A using fixed boundary condition. In Figs. 21 and 22, the

“A-B” lines, respectively, represent the linear and nonlinear elastic deformations using LMM boundary condition. Results show that the elastic deformation using LMM boundary condition is smaller than the response obtained using fixed boundary condition. The response due to gust can be divided into two parts: rigid-body motion and the elastic deformation, which is closer to reality. If the boundary condition of the aircraft wing is regarded as fixed, the gust only results in the elastic deformation of the wing. Because of the total potential of excitation, the response will be larger in fixed boundary condition. It should also be noticed that the displacement response using LMM boundary condition does not become stationary after a certain period, instead it keeps on increasing with the time, as shown in Figs. 18 and 19. This is

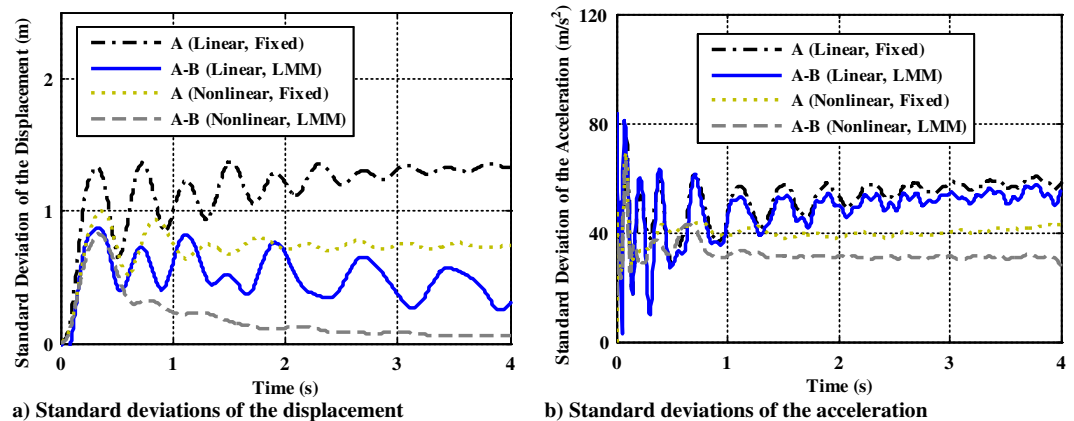


Fig. 21 Results by using LMM and fixed boundary conditions under stationary gust.

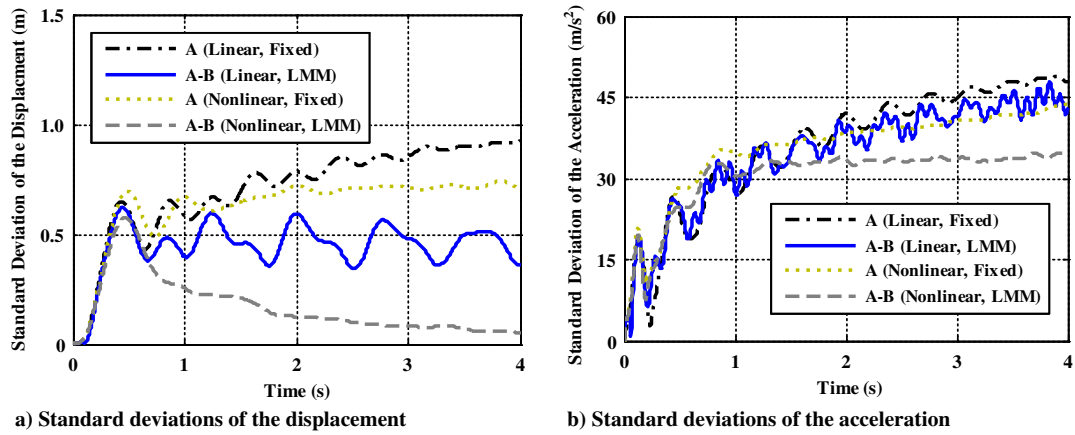


Fig. 22 Results by using LMM and fixed boundary conditions under nonstationary gust.

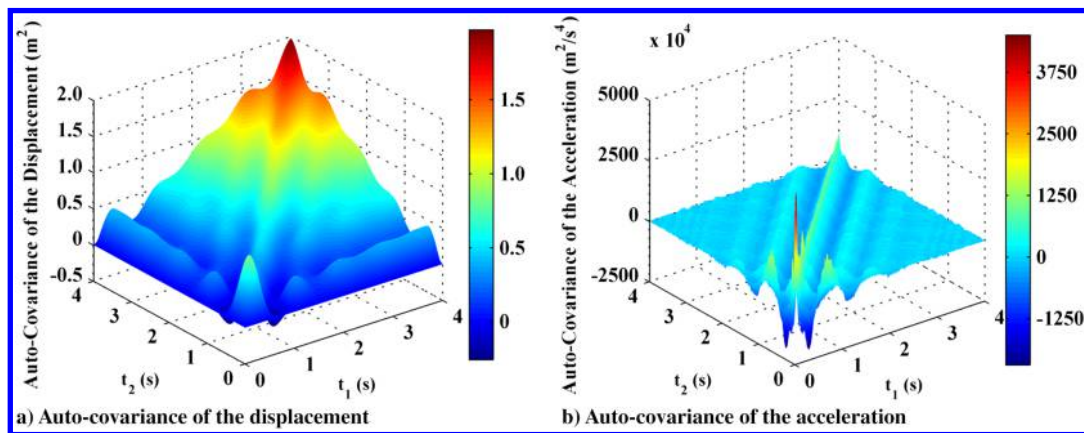


Fig. 23 Autocovariances under partially correlated stationary gust.

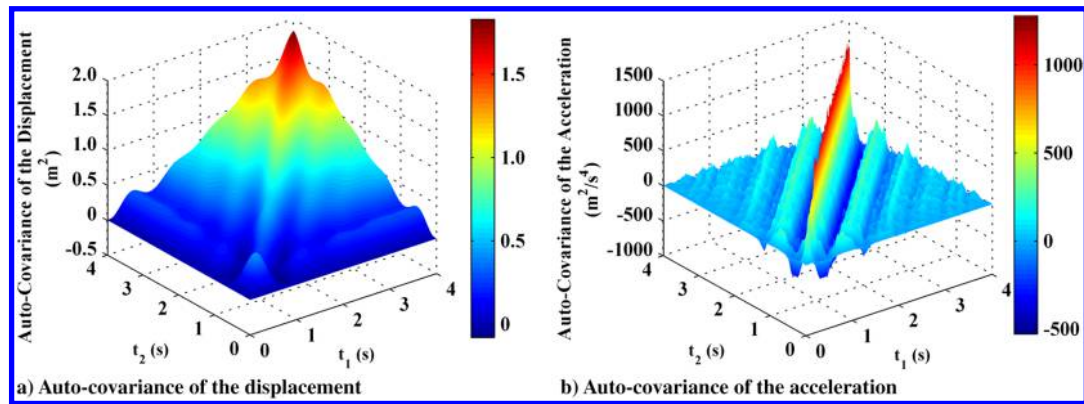


Fig. 24 Autocovariances under partially correlated nonstationary gust.

because the displacement is stationary for the elastic motion, but it continuously increases for the rigid motion. Therefore, it is necessary to model the boundary condition of the wing as an elastic boundary condition by using LMM boundary condition during the design of aircraft. Otherwise, it will result in inaccuracies of the structural response.

The standard deviations of nonlinear displacement and acceleration at point A using LMM boundary condition under partially correlated stationary and nonstationary gust are shown as solid line in Figs. 18 and 19. The corresponding autocovariance of displacement and acceleration at point A are, respectively, plotted in Figs. 23 and 24. We can also notice that the displacements of rigid motion and the

accelerations of elastic deformation dominate the overall response of displacement and acceleration of the wing.

V. Conclusions

A methodology is presented wherein Karhunen-Loeve expansion (KLE), geometric nonlinearity through finite element method (NFEM), and a sampling technique are combined to carry out nonstationary random vibration analysis of complex dynamic systems with geometric nonlinearity where the excitations are correlated random processes both in time and space domains. The eigenvalues and eigenfunctions of the autocovariance are obtained by using orthogonal basis functions.

The KLE for correlated random excitations relies on expansions in terms of the correlated sets of random variables reflecting the cross-covariance of the random excitations. The autocovariance functions of random excitations are discretized into a series of correlated forces that are applied as excitations, and the structural responses are obtained by using NFEM and a sampling technique.

The application of the proposed algorithm is first carried out to a rigid aircraft wing under stationary and nonstationary correlated gusts. To capture the spatial correlation efficiently, the wing is divided into several subdomains, and then the number of subdomains is determined by a convergence study. The response due to correlated random processes is bounded by the response obtained by perfectly correlated and uncorrelated random process excitations. Second, the algorithm is applied to a flexible aircraft wing. The effects of geometric nonlinearity on the magnitude and distribution of structural response are carried out. Results show that the geometric nonlinearity has a hardening effect on the wing response, which suppresses the oscillatory response, and changes the distribution of the responses into non-Gaussian although the excitations are Gaussian. Next, two different types of the boundary conditions of the wing are studied and results compared: 1) fixed boundary condition and 2) LMM boundary condition. The response due to LMM boundary condition, which is closer to reality, is smaller than the response obtained using fixed boundary condition. The proposed methodology can be applied to the analysis of any complex structures and any random excitations. This study will be helpful for the design of aircraft.

Acknowledgments

The work described in this paper was supported by the Jiangsu Natural Science Foundation (BK20170656, BK20170022) and the National Natural Science Foundation of China (11572086, 11402052).

References

- Mulani, S. B., Kapania, R. K., and Scott, K. M. L., "Generalized Linear Random Vibration Analysis Using Autocovariance Orthogonal Decomposition," *AIAA Journal*, Vol. 48, No. 8, 2010, pp. 1652–1661. doi:10.2514/1.J050033
- Hoblitt, F. M., *Gust Loads on Aircraft: Concepts and Applications*, AIAA Education Series, AIAA, Reston, VA, 1988, Chap. 1.
- Ghanem, R., and Spanos, P. D., "A Stochastic Galerkin Expansion for Nonlinear Random Vibration Analysis," *Probabilistic Engineering Mechanics*, Vol. 8, Nos. 3–4, 1993, pp. 255–264. doi:10.1016/0266-8920(93)90019-R
- Roberts, J. B., and Spanos, P. D., *Random Vibration and Statistical Linearization*, Wiley, New York, 2003, Chap. 7.
- Benaroya, H., and Han, S. M., *Probability Models in Engineering and Science*, CRC Press, Boca Raton, FL, 2005, Chap. 6.
- Spanos, P. D., Tezcan, J., and Tratskas, P., "Stochastic Processes Evolutionary Spectrum Estimation via Harmonic Wavelets," *Computer Methods in Applied Mechanics and Engineering*, Vol. 194, No. 12, 2005, pp. 1367–1383. doi:10.1016/j.cma.2004.06.039
- Stefanou, G., "The Stochastic Finite Element Method: Past, Present and Future," *Computer Methods in Applied Mechanics and Engineering*, Vol. 198, No. 9, 2009, pp. 1031–1051. doi:10.1016/j.cma.2008.11.007
- Wirshing, P. H., Paez, T. L., and Keith, O., *Random Vibrations: Theory and Practice*, Dover, New York, 1995, Chap. 5.
- Newland, D. E., *An Introduction to Random Vibrations, Spectral & Wavelet Analysis*, Courier Corp., New York, 2012, Chap. 5.
- Pradlwarter, H. J., Schueller, G. I., and Schenk, C. A., "A Computational Procedure to Estimate the Stochastic Dynamic Response of Large Non-Linear FE-Models," *Computer Methods in Applied Mechanics and Engineering*, Vol. 192, No. 7, 2003, pp. 777–801. doi:10.1016/S0045-7825(02)00595-9
- Choi, S. K., Grandhi, R. V., and Canfield, R. A., *Reliability-Based Structural Design*, Springer-Verlag, London, 2007, Chap. 2.
- Pranesh, S., and Ghosh, D., "Faster Computation of the Karhunen-Loève Expansion Using Its Domain Independence Property," *Computer Methods in Applied Mechanics and Engineering*, Vol. 285, No. 3, 2015, pp. 125–145. doi:10.1016/j.cma.2014.10.053
- Sakamoto, S., and Ghanem, R., "Polynomial Chaos Decomposition for the Simulation of Non-Gaussian Nonstationary Stochastic Processes," *Journal of Engineering Mechanics*, Vol. 128, No. 2, 2002, pp. 190–201. doi:10.1061/(ASCE)0733-9399(2002)128:2(190)
- Phoon, K. K., Huang, S. P., and Quek, S. T., "Implementation of Karhunen-Loève Expansion for Simulation Using a Wavelet-Galerkin Scheme," *Probabilistic Engineering Mechanics*, Vol. 17, No. 3, 2002, pp. 293–303. doi:10.1016/S0266-8920(02)00013-9
- Mulani, S. B., Kapania, R. K., and Walters, R. W., "Karhunen-Loève Expansion of Non-Gaussian Random Process," *48th AIAA/ASME/ASCE/AHS/ASC Structures, Structural Dynamics, and Materials Conference*, AIAA Paper 2007-1943, April 2007.
- Phoon, K. K., Huang, H. W., and Quek, S. T., "Simulation of Strongly Non-Gaussian Processes Using Karhunen-Loève Expansion," *Probabilistic Engineering Mechanics*, Vol. 20, No. 2, 2005, pp. 188–198. doi:10.1016/j.proengmech.2005.05.007
- Li, Y., Mulani, S. B., Scott, K. M. L., Kapania, R. K., Wu, S., and Fei, Q., "Non-Stationary Random Vibration Analysis of Multi Degree Systems Using Auto-Covariance Orthogonal Decomposition," *Journal of Sound and Vibration*, Vol. 372, No. 23, 2016, pp. 147–167. doi:10.1016/j.jsv.2016.02.018
- Scott, K. M. L., "Practical Analysis Tools for Structures Subjected to Flow-Induced and Non-Stationary Random Load," Ph.D. Dissertation, Aerospace and Ocean Engineering Dept., Virginia Polytechnic Inst. and State Univ., Blacksburg, VA, 2011.
- Huang, S. P., Quek, S. T., and Phoon, K. K., "Convergence Study of the Truncated Karhunen-Loève Expansion for Simulation of Stochastic Processes," *International Journal for Numerical Methods in Engineering*, Vol. 52, No. 9, 2001, pp. 1029–1043. doi:10.1002/nme.255
- Tipping, M. E., and Bishop, C. M., "Mixtures of Probabilistic Principal Component Analyzers," *Neural Computation*, Vol. 11, No. 2, 1999, pp. 443–482. doi:10.1162/089976699300016728
- Tipping, M. E., and Bishop, C. M., "Probabilistic Principal Component Analysis," *Journal of the Royal Statistical Society B*, Vol. 61, No. 3, 1999, pp. 611–622. doi:10.1111/rssb.1999.61.issue-3
- Vořechovský, M., "Simulation of Simply Cross Correlated Random Fields by Series Expansion Methods," *Structural Safety*, Vol. 30, No. 4, 2008, pp. 337–363. doi:10.1016/j.strusafe.2007.05.002
- Cho, H., Venturi, D., and Karniadakis, G. E., "Karhunen-Loève Expansion for Multi-Correlated Stochastic Processes," *Probabilistic Engineering Mechanics*, Vol. 34, No. 4, 2013, pp. 157–167. doi:10.1016/j.proengmech.2013.09.004
- Liang, J., Chaudhuri, S. R., and Shinozuka, M., "Simulation of Nonstationary Stochastic Processes by Spectral Representation," *Journal of Engineering Mechanics*, Vol. 133, No. 6, 2007, pp. 616–627. doi:10.1061/(ASCE)0733-9399(2007)133:6(616)
- Shinozuka, M., and Deodatis, G., "Simulation of the Stochastic Process by Spectral Representation," *Applied Mechanics Reviews*, Vol. 44, No. 4, 1991, pp. 191–204. doi:10.1115/1.3119501
- Li, Y., and Kareem, A., "Simulation of Multivariate Nonstationary Random Processes: Hybrid DFT and Digital Filtering Approach," *Journal of Engineering Mechanics*, Vol. 123, No. 12, 1997, pp. 1302–1310. doi:10.1061/(ASCE)0733-9399(1997)123:12(1302)
- Dey, S. S., "Finite Element Method for Random Response of Structures due to Stochastic Excitation," *Computer Methods in Applied Mechanics and Engineering*, Vol. 20, No. 2, 1979, pp. 173–194. doi:10.1016/0045-7825(79)90016-1
- Yang, T. Y., and Kapania, R. K., "Finite Element Random Response Analysis of Cooling Tower," *Journal of Engineering Mechanics*, Vol. 110, No. 4, 1984, pp. 589–609. doi:10.1061/(ASCE)0733-9399(1984)110:4(589)
- Ghanem, R. G., and Spanos, P. D., *Stochastic Finite Elements: A Spectral Approach*, Courier Corp., New York, 2003, Chap. 2.
- Mulani, S. B., Kapania, R. K., and Walters, R. W., "Stochastic Eigenvalues Problem with Polynomial Chaos," *47th AIAA/ASME/ASCE/AHS/ASC Structures, Structural Dynamics, and Materials Conference*, AIAA Paper 2006-2068, May 2006.
- Zhang, J., and Ellingwood, B., "Orthogonal Series Expansions of Random Fields in Reliability Analysis," *Journal of Engineering Mechanics*, Vol. 120, No. 12, 1994, pp. 2660–2677. doi:10.1061/(ASCE)0733-9399(1994)120:12(2660)

- [32] *Implicit Nonlinear (SOL 600) User's Guide*, Nastran, M. D., Los Angeles, Jan. 2006, <http://www.mscsoftware.com/course/implicit-nonlinear-analysis-using-msc-nastran-sol600> [retrieved 2016].
- [33] Howell, L. J., and Lin, Y. K., "Response of Flight Vehicles to Nonstationary Atmospheric Turbulence," *AIAA Journal*, Vol. 9, No. 11, 1971, pp. 2201–2207. doi:10.2514/3.50026
- [34] Lee, J., "The Plunging-Mode Response of an Idealized Airplane to Atmospheric Turbulent Gusts," *Journal of Sound and Vibration*, Vol. 44, No. 1, 1976, pp. 47–62. doi:10.1016/0022-460X(76)90706-9
- [35] Dimitriadis, G., "Design Loads for Future Aircraft," NATO RTO-TR-045, Canada, 2002.
- [36] Barnes, T. J., and Warman, R. M., "Aircraft Load due to Turbulence and Their Impact on Design and Certification," NATO AGARD-R-798, Brussels, 1994.
- [37] Nigam, N. C., and Narayanan, S., *Applications of Random Vibrations*, Springer-Verlag, New York, 1994, Chap. 5.
- [38] Liu, Q., Jrad, M., Mulani, S. B., and Kapania, R. K., "Integrated Global Wing and Local Panel Optimization of Aircraft Wing," *56th AIAA/ASME/ASCE/AHS/ASC Structures, Structural Dynamics, and Materials Conference*, AIAA Paper 2015-0137, Jan. 2015.
- [39] Kim, Y. W., and Jung, M. J., "A Study on Large Mass Method for Dynamic Problem of Multiple Degree-of-Freedom System Excited by Ground Acceleration Time History," *Journal of Mechanical Science and Technology*, Vol. 28, No. 1, 2014, pp. 25–41. doi:10.1007/s12206-013-0941-x
- [40] Kim, Y. W., and Jung, M. J., "Mathematical Analysis Using Two Modeling Techniques for Dynamic Responses of a Structure Subjected to a Ground Acceleration Time History," *Nuclear Engineering and Technology*, Vol. 43, No. 4, 2011, pp. 361–374. doi:10.5516/NET.2011.43.4.361
- [41] Pebesma, E. J., and Heuvelink, G. B. M., "Latin Hypercube Sampling of Gaussian Random Fields," *Technometrics*, Vol. 41, No. 4, 1999, pp. 303–312. doi:10.1080/00401706.1999.10485930